Contributions to Mineralogy and Petrology (2025) 180:55
https://doi.org/10.1007/s00410-025-02244-2

ORIGINAL PAPER

Authigenic growth of monazite, xenotime, rutile and zircon by fluid-rock interaction in the Southern Serra do Espinhaço, Brazil

Armin Zeh[1] · Stephanie Lohmeier[2] · Alexandre Raphael Cabral[3] · Axel Gerdes[4] · Kirsten Drüppel[1]

Received: 8 February 2025 / Accepted: 16 July 2025 / Published online: 1 August 2025

Abstract

The minerals zircon, monazite, xenotime and rutile commonly occur in metasedimentary rocks as detrital but also authigenic grains, which can result from different fluid-driven processes. In this study such processes are investigated on the basis of detailed petrographic observations, mineral-geochemical data, and results of in situ U-Pb dating and Nd isotope analyzes in a kaolinitized micaschist. The data provide evidence for the preservation of detrital grains of zircon, rutile and monazite crystallized between ~3100 and 1150 Ma, and for authigenic zircon, xenotime, rutile and monazite formed at ca. 530 Ma. The authigenic character is indicated by zircon outgrowths closely intergrown with xenotime and rutile crystals. The outgrowths occur where detrital zircon faces are intensely dissolved in contact with Fe-Mg-rich phengitic muscovite, suggesting the involvement of an aqueous fluid enriched in K-Mg-Fe-Al-Ti-P near the thermal peak at 510 °C and >0.8 GPa. In contrast, authigenic monazite rims overgrowing rounded cores were formed during the retrograde evolution, as indicated by their occurrence in assemblage with kaolinite, and results of geothermobarometry (T = 280 °C, P < 0.3 GPa). The monazite rims show very low U contents (4–14 µg/g), extremely high Th/U (up to 1670), and nearly identical $^{143}Nd/^{144}Nd_t$ (0.51184 ± 0.00006) values that markedly differ from those of the detrital cores ($^{143}Nd/^{144}Nd_t$ = 0.51000 ± 0.00050; U = 162–16418 µg/g; Th/U = 2.6–153). The high Th/U points to the involvement of an oxidizing fluid, in line with late goethite formation. Monazite microstructures, and Nd isotope characteristics require a chain of processes, from partial dissolution of detrital monazite, through REE transport and Nd isotope homogenization in an aqueous fluid, to new monazite growth.

Keywords Monazite · Xenotime · Rutile · Zircon · Fluid-rock interaction · U-Pb dating · Geothermobarometry

Introduction

The minerals zircon, monazite, xenotime and rutile are the major hosts for high-field strength elements (HFSE) and rare earth elements (REE) in most sedimentary, metamorphic and magmatic rocks, and are commonly used to constrain the age of magmatic, metamorphic, diagenetic and hydrothermal events (e.g., Black and Williams 1986; Rasmussen 2005; Zack et al. 2011; Janots et al. 2012; Lan 2022). All four minerals can survive mechanical abrasion and chemical alteration, but their preservation potential is different and dependent on a wide range of conditions and processes. Detrital zircon and rutile are most resistant during weathering, mechanical transport and fluid-rock interaction (e.g., Hubert 1962; Morton and Hallsworth 1994; Andò et al. 2012; Lan 2022). Detrital rutile has a great preservation potential until lower-amphibolite-facies conditions and zircon until granulite-facies conditions (e.g., Meinhold 2010;

Communicated by Daniela Rubatto.

✉ Armin Zeh
armin.zeh@kit.edu

[1] Institute for Applied Geosciences, Mineralogy and Petrology, KIT - Karlsruhe Institute of Technology, Adenauerring 20b, Geb. 50.4, 76131 Karlsruhe, Germany

[2] Institute for Geotechnology and Mineral Resources, Technische Universität Clausthal, Adolph-Roemer Strasse 2A, 38678 Clausthal-Zellerfeld, Germany

[3] Independent exploration geologist, Belo Horizonte, MG, Brazil

[4] Frankfurt Isotope and Element Research Center (FIERCE), Goethe-University Frankfurt, 60438 Frankfurt am Main, Germany

Zeh et al. 2010a, b; 2018, and references therein). Although detrital populations of both minerals can quantitatively be transformed into authigenic (in situ formed) populations by fluid-driven alteration under conditions much lower than their respective closure temperatures. For the U-Pb system the closure temperatures are at >900 °C for zircon, xenotime and monazite (Cherniak and Watson 2001; Cherniak et al. 2004; Cherniak 2006), and at 600 °C for rutile (Cherniak 2000), for crystals of approximately 100 µm in diameter and geological meaningful cooling rates. Fluid-driven alteration can result from two distinct processes: (1) CDR (**C**oupled **D**issolution-**R**eprecipitation; e.g., Putnis 2002; Putnis and Putnis 2007; Geisler et al. 2007), causing in situ replacement of grains along reaction fronts, and (2) DTR, which comprises **D**issolution of grains, followed by distant **T**ransport of HFSE species on hand-specimen scale or even beyond, and **R**eprecipiation of new authigenic grains of the same species. For rutile, both processes have been demonstrated by Zeh et al. (2018), for zircon by a number of field-based studies (e.g., Rasmussen 2005; Geisler et al. 2007; Hay and Dempster 2009; Hay et al. 2010; Zeh et al. 2010a, b; Bojanowski et al. 2012), and for monazite and/or xenotime by Rasmussen et al. (2002), Harlov et al. (2011), and Allaz et al. (2013). The preservation potential for detrital monazite and xenotime during sediment transport and diagenesis is commonly much lower compared to zircon and rutile (e.g., Morton and Hallsworth 2007), as reflected by their relatively rare occurrence in modern-day river and beach sands (e.g., Andò et al. 2012), as well as in diagenetically overprinted fluvial to shallow marine rocks (e.g., Morton and Hallsworth 1994), although there are spectacular exceptions such as the monazite sands of India and Brazil (e.g., Sengupta and van Gosen 2016).

In metasedimentary rocks, detrital monazite and xenotime are commonly altered during the interaction with aqueous fluids under low- to medium-grade metamorphic conditions, although there are several examples reporting both detrital and authigenic monazite and xenotime in siliciclastic sedimentary rocks in fluvial and non-fluvial environments (e.g., Allaz et al. 2013; Lan et al. 2014; Zhang et al. 2015; Lan 2022; Zhang et al. 2022, and references therein). Alteration is commonly expressed by changes in original chemical compositions and ages (e.g., Allaz et al. 2013; Lan et al. 2014; Berry et al., 2018). Furthermore, it is well documented that detrital monazite can survive medium- and even high-grade metamorphic conditions (e.g., Copeland et al. 1988; Zeh et al. 2004; Baldwin et al., 2006; Rasmussen and Muhling 2007, and references therein). In addition, both xenotime and monazite can newly form at the expense of other REE-bearing phases, e.g. xenotime at the expense of zircon (e.g., Lan et al. 2014; Franz et al. 2015), or monazite at the expense of allanite (e.g., Krenn and Finger 2007). Alternatively, monazite can form also during garnet breakdown at certain bulk compositions and pressure-temperature conditions (e.g., Spear and Pyle 2010).

In this study, zircon, monazite, rutile and xenotime grains are investigated in an intensely kaolinized micaschist that forms a layer within the diamond-bearing metaconglomerate of the Sopa-Brumadinho Formation, stratigraphically designated to the Upper Espinhaço Group (Chemale et al., 2012). Combined results of detailed petrography, mineral chemistry, in situ U-Pb dating and Sm-Nd isotope analyzes provide new information on the timing of sediment deposition and metamorphic-hydrothermal overprint, as well as on the pressure-temperature conditions and the fluid regime during the authigenic growth of HFSE minerals.

Analytical techniques

A hand-specimen sample of micaschist was investigated by a number of analytical techniques on polished (thin) sections, sample powders and heavy-mineral concentrates. The analytical techniques comprise polarization microscopy, scanning electron microscopy (SEM) coupled with EDX (energy-dispersive X-ray detector), Raman spectroscopy, and X-ray diffraction (XRD), as well as laser ablation - inductively coupled plasma - mass spectrometry (LA-ICP-MS), performed at the Department of Mineralogy and Petrology at the Karlsruhe Institute of Technology (KIT), and at FIERCE Frankfurt am Main (Germany). In addition, quantitative mineral analyzes were carried out by electron-probe microanalyzes (EPMA) at the Department of Geosciences, working group Geochemistry-Petrology-Economic Geology at the Clausthal University of Technology (Germany). Detailed information on analytical techniques and conditions are presented in the electronic supplementary material (ESM), which also records the results of U-Pb dating and trace-element analyzes by LA-ICP-MS (Tables S1, S2 and S3), mineral chemistry by EPMA (Table S4), and in situ Sm-Nd isotope analyzes (Table S5).

Sample material and petrography

The sample material is a micaschist, taken from a steeply dipping, well foliated layer of approximately 50 cm in thickness within the Sopa-Brumadinho metaconglomerate forming part of the Upper Espinhaço Group in the southern Serra do Espinhaço (Chemale et al. 2012). The sample location is the historical Extração diamond mine, also known as Curralinho (Moraes and Guimarães 1931), which occurs about 10 km southeast of Diamantina. The sampling-site coordinates are as follows: 18°17'46.65"S, 43°31'17.59"W. The

schist layer dips 75° towards the azimuth 040°. The layer is predominately made up by white mica, intercalated by millimeter-thick layers and lenticular aggregates of quartz. Quartz grains commonly show 120° triple point junctions (Fig. 1a), indicative of static recrystallization at temperatures above 400 °C (e.g., Stipp et al. 2002), which is also supported by the nearly absence of quartz grains with undulatory extinction and/or subgrain boundaries (Fig. 1b). Both quartz and white mica are closely intergrown with rutile crystals of different shape. Subangular rutile grains point to a detrital origin (Fig. 2a), and rutile agglomerates in mica-rich domains to coalescence of a large number of tiny rutile crystals (Figs. 1e, f and 2c). Most quartz grains contain tiny rutile needles of sub-micrometer diameter (Fig. 1c), and are closely intergrown with reddish-brownish crystals of goethite of up to 200 µm in length (Fig. 1d, h). We note that goethite occurs widespread in quartz-rich domains, but is less frequently found together with tourmaline in mica-rich domains (Fig. 1h), particularly in domains where white mica is intergrown with kaolinite (Fig. 1g). Kaolinite forms very fine-grained crystalline aggregates showing greyish-whitish interference colors in cross-polarized light (Fig. 1g). The mineral was unambiguously identified as kaolinite by X-ray diffraction, together with quartz, muscovite, rutile and goethite (Fig. S2 in electronic supplementary materials - ESM). The identification of rutile, muscovite and goethite were further corroborated by Raman spectroscopy (ESM Fig. S1).

Zircon and monazite grains, rarely observed in thin sections, are abundant in heavy-mineral concentrates together with rutile and more seldom with xenotime. Backscattered-electron (BSE) images, along with results of mineral chemistry, in situ U-Pb dating and Nd isotope analyzes (see section: Results), provide evidence for the authigenic nature of zircon, rutile, monazite and xenotime, but also for the preservation of detrital zircon, rutile, and monazite grains. The latter is illustrated in BSE images showing rounded detrital cores of zircon and monazite surrounded by newly formed rims (Figs. 2g, h and 3e). Furthermore, they reveal that approximately 95% of the detrital zircon grains were intensely leached at their surfaces in contact with muscovite (ESM-Figs. S3 and S4), leaving angular, box-like pits, up to 10 µm in length, surrounded by walls of newly formed zircon (Fig. 3a, b). In polished epoxy mounts these walls appear as outgrowths around pristine (Fig. 3e) or strongly

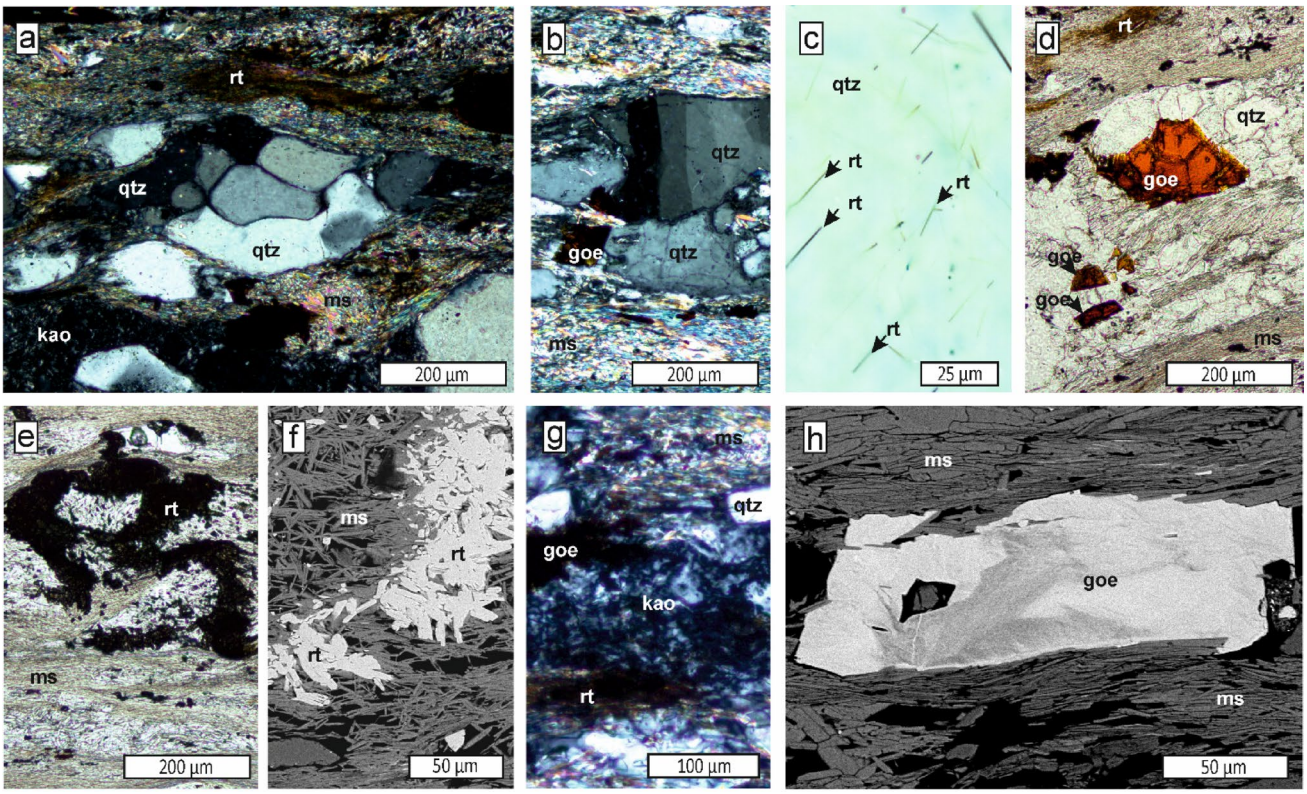

Fig. 1 Microstructural relationships revealed by photomicrographs (**a**–**e**, **g**), and BSE images (**f**, **h**). **a** Sigma-shaped cluster of statically recrystallized quartz grains (qtz) with 120° triple point contacts, surrounded by muscovite (ms) intercalated with nests of tiny rutile grains (rt). The lower-left part is dominated by a pocket filled with kaolinite (kao). **b** Recrystallized quartz with subgrain boundaries in contact with muscovite and goethite (goe). **c** Quartz crystal enclosing rutile needles. **d** Goethite crystals in a quartz-rich domain. **e**, **f** Accumulation of rutile needles in a muscovite-dominated matrix. **g** Kaolinite-dominated domains in contact with quartz, rutile, goethite and muscovite. **h** Goethite crystal in a muscovite matrix. Brightness variations result from different Al-content in goethite

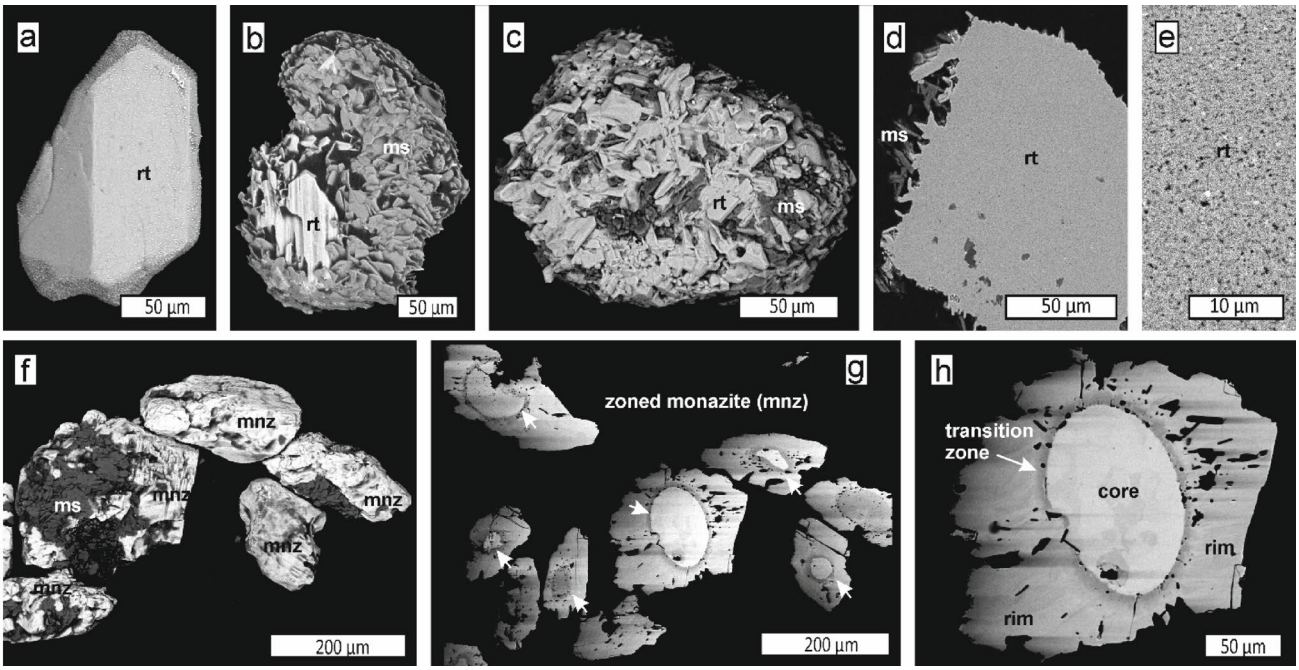

Fig. 2 BSE images of rutile (**a–e**) and monazite (**f–h**). **a** Detrital rutile grain (rt) of angular shape, **b** authigenic rutile crystal with striations closely intergrown with muscovite (ms), **c** morphology and **d** polished section of a hedgehog-shaped authigenic rutile aggregate, **e** internal structure of authigenic rutile showing abundant nanopores (black dots) and secondary mineral inclusions (bright dots). **f** Morphology of authigenic monazite grains (mnz) intergrown with muscovite, (**g**, **h**). Internal structures of monazite grains reveal round cores of detrital origin overgrown by authigenic rims, with a small transition zone in between (highlighted by BSE contrast and tiny inclusions - arrows)

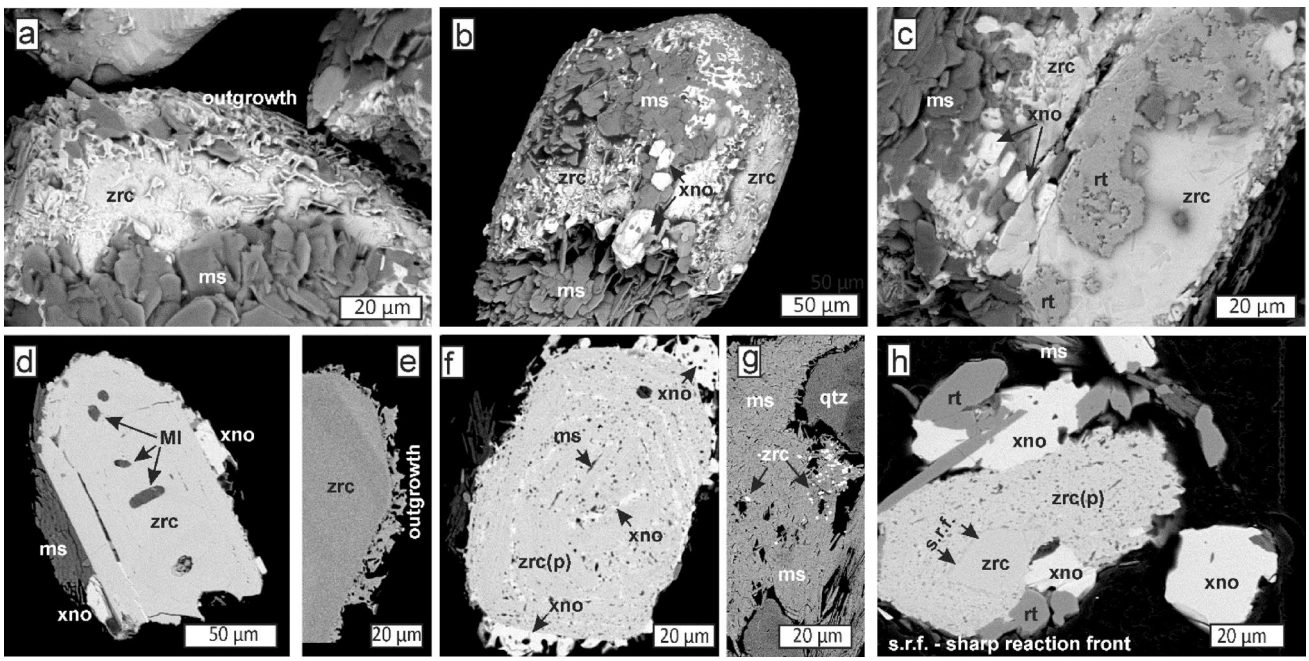

Fig. 3 BSE images of zircon grains. **a** Surface of a detrital zircon grain (zrc) decorated with zircon outgrowths between adjacent muscovite (ms) crystals. **b**, **c** Surface of altered zircon grains intergrown with muscovite, authigenic xenotime (xno) and rutile (rt). Polished sections of pristine (**d**, **e**) and altered (**f**, **h**) detrital zircon grains. Pristine grains commonly contain melt inclusions (MI) and/or apatite, altered grains show microporous textures [zrc(p)] filled with xenotime and muscovite. Detrital zircon grains are commonly surrounded by zircon outgrowths of < 10 µm width (**e**), intergrown with authigenic xenotime and rutile (**f**, **h**). **g** Spray of authigenic zircon grains in a muscovite matrix

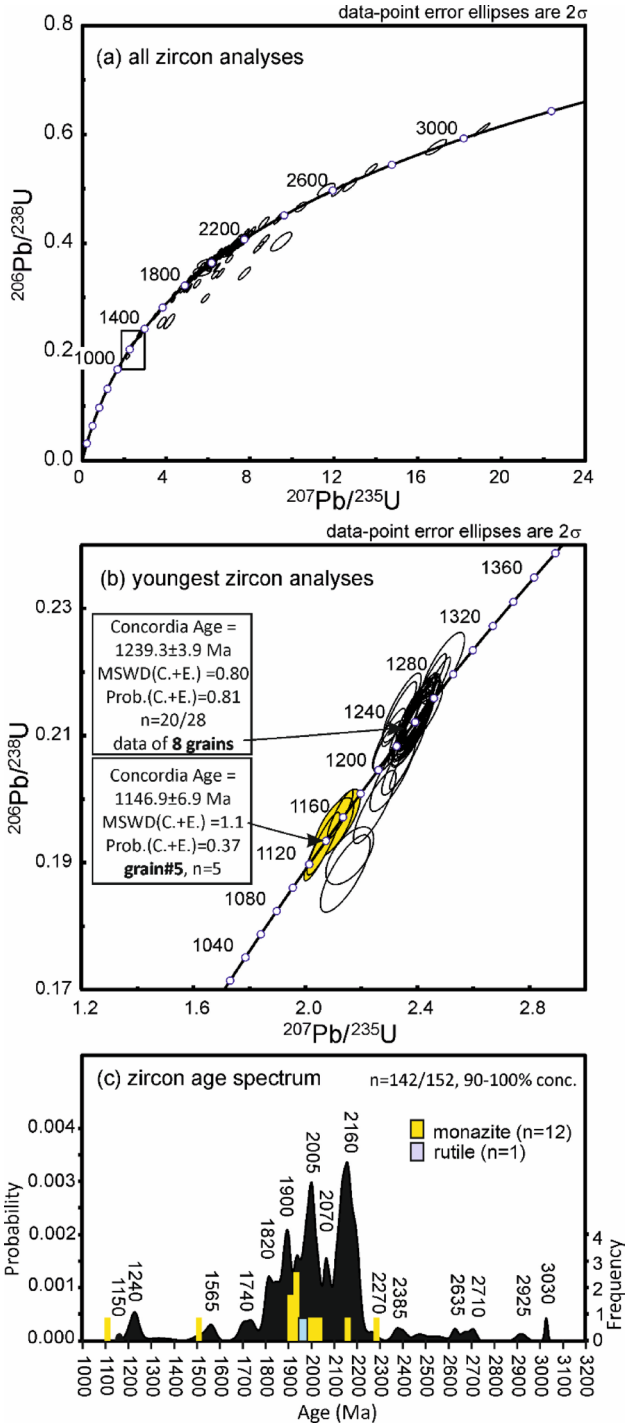

Fig. 4 Results of U-Pb dating of detrital zircon grains. **a** Concordia diagrams showing the results of all dated zircon grains, and **b** U-Pb ages of the youngest detrital zircon grains derived by multiple analyzes. **c** Age spectrum of detrital zircon grains vs. relative probability. The frequencies of ages of detrital monazite and rutile grains are shown for comparison

altered (Fig. 3f, h) detrital zircon cores. The zircon outgrowths never exceed 10 µm in length and are commonly intergrown with xenotime and rutile (Fig. 3b–d, f, h). Xenotime is also located along zircon fractures and in porous domains (Fig. 3f, h), which in some crystals follow the former zircon growth zoning (Fig. 3f). Locally, sprays of tiny zircon grains (<1 µm diameter) were found in muscovite-rich domains (Fig. 3g).

Rutile grains, recovered from the heavy-mineral concentrate, are commonly intergrown with muscovite (Fig. 2b–d), and only a few grains show angular crystal faces (Fig. 2a). Most grains form hedgehog-shaped aggregates with a relatively homogeneous core domain surrounded by crystals of acicular-tabular habit (Fig. 2c, d). At high magnification, BSE images reveal nanopores and very tiny, secondary mineral inclusions, <<1 µm across, within most rutile grains and aggregates (Fig. 2e).

Monazite grains are up to 250 µm across and show rough surfaces. The mineral is commonly intergrown with muscovite and rutile (Fig. 2f; ESM-Fig. S5). Rarely, monazite was also observed in kaolinite-bearing domains. In polished epoxy mounts, most monazite grains show round cores overgrown by rims of irregular shape (Fig. 2g, h), containing abundant inclusions of white mica. In most grains, the rims are thicker than the cores, and the core-rim transition is highlighted by a BSE-dark, inclusion-rich zone (Fig. 2g, h). Xenotime crystals are mostly round and show a faint patchy zoning in high-contrast BSE images. They rarely exceed 40 µm diameter, and commonly occur intergrown with zircon (Fig. 3b–d, h), but have nowhere been observed in direct contact with monazite.

Results of U-Pb dating

Zircon

During this study 154 detrital zircon grains were dated in situ by LA-ICP-MS, 134 grains of which yielded concordant ages between 3032 and 1147 Ma (concordance level = 90–110%). Most grains show oscillatory zoning and Th/U ratios > 0.2 (min. = 0.13, max. = 1.8, median = 0.56; $n = 152$), typical of magmatic zircon grains. The age spectrum reveals a predominant Paleoproterozoic population with several age peaks between 2160 and 1820 Ma (Fig. 4a, c). In addition, there is a significant number of older grains with minor peaks between 3030 and 2270 Ma, and younger grains with peaks at 1740, 1550 and 1240 Ma. The ages of the youngest grains (<1250 Ma) are confirmed by multiple analyzes (Fig. 4b; ESM Table S1). Five analyzes of zircon grain #5 returned a concordia age of 1146.9 ± 6.9 Ma, and multiple analyzes of eight grains a concordia age of

1239.3 ± 3.9 Ma (20 out of 28 analyzes), coinciding with the youngest age peak. Zircon outgrowths could not be dated because of their small size of ≤ 10 µm across and the presence of abundant inclusions of rutile and xenotime (Fig. 3a, e).

Monazite and xenotime

Twenty-six core and 70 rim domains were analyzed from a total of 43 monazite grains. For twelve grains of monazite both cores and rims were analyzed (ESM Table S2). Monazite cores consistently show higher U and Pb contents (U = 176–11214 µg/g, Pb = 1528–16228 µg/g; n = 26), and much lower Th/U ratios (9–144) and common Pb (^{206}Pb comm = below detection to 7.6%), compared to monazite rims (U = 7–20 µg/g, Pb = 209–567 µg/g, Th/U = 662–1364, ^{206}Pb comm = 3.5–86%; n = 69). The cores yield concordant to nearly concordant ^{207}Pb/^{206}Pb ages between 2300 and 1150 Ma (Fig. 5a). For some grains the core age was constrained by multiple analyzes (up to 4)– e.g., grains g22c and g42c (Fig. 5c, d). Monazite rims consistently gave highly discordant ages, due to high level of common Pb. In the Tera-Wasserburg diagram, most analyzes define a regression line with a lower intercept age at 531 ± 27 Ma (Fig. 5b), overlapping with a weighted mean ^{207}Pb/^{206}Pb age of 531.0 ± 3.4 Ma, obtained from 4 xenotime grains (Fig. 4e). We note that the xenotime grains have much higher U contents (U = 93–657 µg/g) and much lower Th/U ratios (5.6–14), and common Pb ($^{206}Pb_{com}$ mostly between 1.9 and 6.2%; n = 14), compared to the monazite rims.

Rutile

Nine rutile grains were analyzed. Only one of these grains (#g1) yielded a concordant age of 1964 ± 7 Ma. All other analyzes are highly discordant (Fig. 5f; ESM Table S2), and provide no meaningful age information. We note that grain #g1 is characterized by angular crystal faces (Fig. 2a), very low Th/U (0.01) and common Pb (0.31%), whereas all other grains show acicular-tabular habit in hedgehog-shaped aggregates (Fig. 2c, d), with significantly higher Th/U ratios (0.09–5.46) and common Pb content (^{206}Pb comm = 14–98%). In combination, the rutile microstructures and the results of U-Th-Pb dating suggest a detrital origin for the angular grain #g1, whereas all other grains were significantly modified or newly formed during metamorphic overprint (see section: Discussion).

Fig. 5 Results of U-Pb dating of **a–d** monazite, **e** xenotime, and **f** rutile. **a**, **b** Tera-Wasserburg diagrams showing the results of **a** detrital monazite cores and **b** authigenic monazite rims. Xenotime data in **b** are shown for comparison. **c**, **d** U-Pb ages obtained by multiple dating of detrital monazite cores. **e** weighted mean ^{206}Pb/^{238}U age of the 15 most concordant xenotime analyzes. **f** Results of rutile dating. The concordant age at ca. 1.96 Ga is obtained from a detrital rutile grain, whereas authigenic grains show a wide scatter

Results of mineral chemistry

The minerals quartz, muscovite, rutile, monazite and xenotime were analyzed by EPMA and LA-ICP-MS for major and trace-element contents. The results are shown in ESM Tables S3 and S4.

Quartz

Fifty grains of quartz, between 200 and 500 µm across, were randomly selected for LA-ICP-MS analyzes on a polished epoxy mount. Only 21 grains yielded reliable results because of shattering or unsteady signals during laser ablation, either due to bad laser-quartz coupling, or drilling into inclusions. Based on the Al content, two groups of quartz can be distinguished. Quartz of group I has comparatively low Al contents, < 75 µg/g (median = 14 µg/g; n = 9), whereas that of group II has > 179 µg/g Al (median = 355 µg/g; n = 12; ESM Table S3). Group-I quartz also shows lower contents in Li (median = 1.8 µg/g), Na (12 µg/g), La (0.02 µg/g), Pb (1.6 µg/g) and Ti (8.9 µg/g), compared to group-II quartz (Li = 29 µg/g, Na = 74 µg/g, Pb = 8.0 µg/g, La = 0.21 µg/g, Ti = 37 µg/g). Application of the Ti-in-quartz geothermometer of Wark and Watson (2006) gives temperatures between 453 and 549 °C for group-I quartz (mean = 509 ± 40 °C; n = 9), and between 621 and 731 °C for group-II quartz (mean = 674 ± 46 °C; n = 12).

Muscovite

Seven muscovite grains on a polished mount were measured by EPMA, mostly crystals that are closely intergrown with grains of rutile and zircon (ESM Table S4). All 28 analyzes, normalized to 11 atoms of oxygen, show high contents of Si (3.28 to 3.65 a.p.f.u.– atoms per formula unit; median = 3.48), Mg (0.22 to 0.59 a.p.f.u.; median = 0.32), and Fe (0.27 to 0.35 a.p.f.u.; median = 0.31), and low contents of Al (1.77 to 2.11 a.p.f.u.; median = 1.92). The X_{Fe} ratio [molar Fe^{2+}/(Fe^{2+}+Mg)] ranges from 0.34 to 0.51, and the Ti contents are between 0.43 and 1.63 wt% (median = 0.82 wt%). The results of EPMA indicate a high degree of Tschermak´s substitution [$Si^{4+}(Fe^{2+},Mg^{2+}) \Leftrightarrow 2\ Al^{3+}$], and show that muscovite has a high component of phengite (X_{phe} = 0.41–0.58), and a very low component of paragonite (X_{pa} = < 0.02). The results further suggest that some muscovite grains were

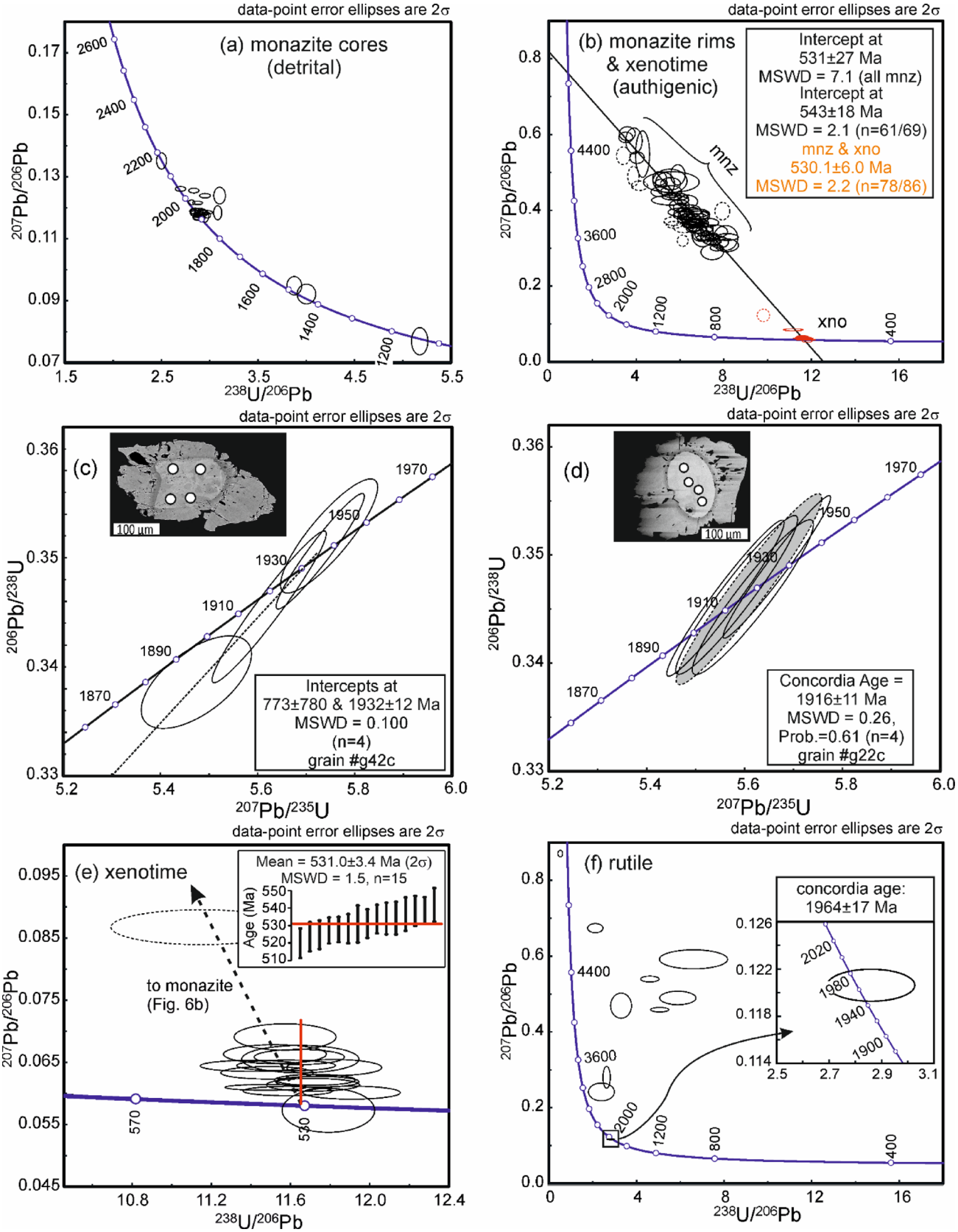
data-point error ellipses are 2σ
(a) monazite cores (detrital)
2600
2400
2200
2000
1800
1600
1400
1200
$^{207}Pb/^{206}Pb$
$^{238}U/^{206}Pb$
data-point error ellipses are 2σ
(b) monazite rims & xenotime (authigenic)
Intercept at 531±27 Ma
MSWD = 7.1 (all mnz)
Intercept at 543±18 Ma
MSWD = 2.1 (n=61/69)
mnz & xno
530.1±6.0 Ma
MSWD = 2.2 (n=78/86)
mnz
xno
4400
3600
2800
2000
1200
800
400
$^{207}Pb/^{206}Pb$
$^{238}U/^{206}Pb$
data-point error ellipses are 2σ
(c)
100 µm
1970
1950
1930
1910
1890
1870
Intercepts at 773±780 & 1932±12 Ma
MSWD = 0.100
(n=4)
grain #g42c
$^{206}Pb/^{238}U$
$^{207}Pb/^{235}U$
data-point error ellipses are 2σ
(d)
100 µm
1970
1950
1930
1910
1890
1870
Concordia Age = 1916±11 Ma
MSWD = 0.26,
Prob.=0.61 (n=4)
grain #g22c
$^{206}Pb/^{238}U$
$^{207}Pb/^{235}U$
data-point error ellipses are 2σ
(e) xenotime
Mean = 531.0±3.4 Ma (2σ)
MSWD = 1.5, n=15
Age (Ma)
550
540
530
520
510
to monazite (Fig. 6b)
570
530
$^{207}Pb/^{206}Pb$
$^{238}U/^{206}Pb$
data-point error ellipses are 2σ
(f) rutile
concordia age: 1964±17 Ma
2020
1980
1940
1900
4400
3600
2000
1200
800
400
$^{207}Pb/^{206}Pb$
$^{238}U/^{206}Pb$

considerably affected by retrograde alteration, as indicated by low K_2O+Na_2O (<10 wt%). This alteration presumably led to the formation of kaolinite, as determined by XRD (ESM Figure S2).

Rutile

Six randomly selected rutile grains were measured by EPMA (18 spots), either hedgehog-shaped aggregates or independent acicular-tabular crystals. All analyzes indicate nearly pure TiO_2 composition, with minor impurities of FeO (0.44–1.68 wt%; median = 0.71; n = 18), and SiO_2 (median = 0.06 wt%). Measurements for trace elements by LA-ICP-MS additionally reveal that grains and aggregates of authigenic rutile have much higher contents of Al (242–4463 µg/g), Nb (1192–2049 µg/g), and ^{208}Pb (33–742 µg/g), compared to the detrital rutile (only one analyzis: Al = 35 µg/g; Nb = 795 µg/g; ESM Tables S3 and S4). The Zr content of the authigenic rutile is highly variable and ranges from 26 to 398 µg/g, while the detrital grain has 168 µg/g. We note that the authigenic rutile grains contain significant amounts of Th (7–97 µg/g), REE (ΣREE = 48–3560 µg/g), and Y (26–239 µg/g), as well as unusually high Th/U ratios (1.2 to 4.2), whereas most of these elements are below the detection limit in the detrital grain. The latter has, on the other hand, the highest contents of W (4787 µg/g) and V (1574 µg/g). Based on CI-chondrite-normalized REE patterns, three types of authigenic rutile can be distinguished, all with slightly negative Eu anomalies [$Eu^*_N = Eu_N/(Sm_N+Gd_N)/2$], ranging from 0.71 to 0.89 (Fig. 6c; ESM Table S3). Type-1 rutile is characterized by an enormous decrease from light to heavy REE (respectively, LREE and HREE), as indicated by $(Sm/Yb)_N$ = 47; type-2 rutile has a comparatively moderate fractionation trend with $(Sm/Yb)_N$ from 3.3 to 4.1; and type-3 rutile displays a positive fractionation trend with $(Sm/Yb)_N$ from 0.18 to 0.59.

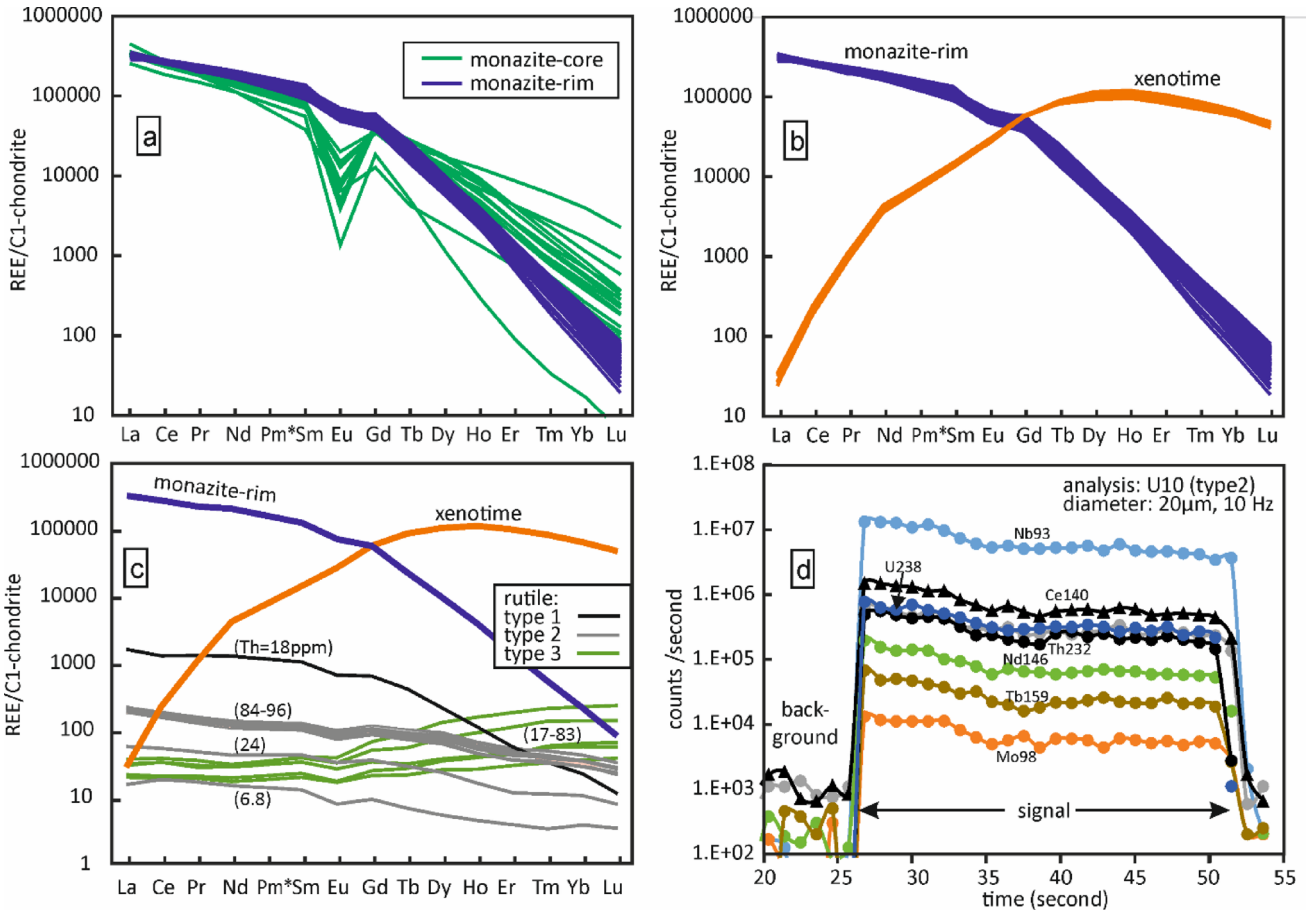

Fig. 6 Results of rare earth element (REE) analyzes of monazite, xenotime and rutile by LA-ICP-MS. **a**, **b** CI-chondrite normalized REE patterns for detrital monazite cores, authigenic monazite rims and xenotime. **c** CI-chondrite normalized REE patterns of authigenic rutile analyzes compared to authigenic monazite and xenotime. Based on these patterns three types of authigenic rutile are distinguished, as explained in text. Numbers in round brackets reflect the Th content (in µg/g) analyzed. **d** Time-resolved signal of an authigenic rutile of type 2 obtained by LA-ICP-MS with a spot diameter of 20 µm and a pulse rate of 10 Hz. Note the parallel trend of rutile-compatible and -incompatible elements (for explanations see text)

Monazite

Most monazite grains are zoned and show round cores of detrital origin with ages between 1.1 and 2.3 Ga, surrounded by rims of irregular morphologies that formed at ca. 530 Ma (Figs. 2g and 5c, d). The core-rim transition is commonly sharp, with a small transition zone, as indicated by BSE images and zoning profiles (Figs. 2h and 7a–m). Cores and rims of 32 monazite grains were analyzed by EMPA (ESM Table S4) and LA-ICP-MS (ESM Table S3) for major and trace elements, respectively, and additionally for Nd isotopes (ESM Table S5).

The analyzes reveal a wide range in composition for the cores, and a more limited range for the rims, as indicated by CI-chondrite-normalized REE patterns (Fig. 6a), as well as compositional variations of several trace elements (Fig. 7d–l, n–q), and initial $^{143}Nd/^{144}Nd$ ratios (Fig. 7m, r). The cores consistently have much higher contents of U (cores = 2272 µg/g; rims = 8.3 µg/g; all values are median), Th (cores = 3.9 wt%, rims = 0.88 wt%), and Ca (cores = 7665 µg/g; rims = 2080 µg/g), and much lower contents of As (cores = 633 µg/g; rims = 1390 µg/g), compared to the rims. Furthermore, the cores show remarkably lower Th/U ratios (cores = 18; rims = 1057), smaller Eu anomalies (Eu^*_N of cores = 0.14; rims = 0.79), and greater variations in REE fractionation patterns (La/Lu_N of cores = 142–10863; rims = 3660–16295). The initial $^{143}Nd/^{144}Nd$ ratios of the cores vary significantly from 0.50944 to 0.51055 (n = 15), corresponding to εNd_t between −11.6 and 4.3, while the rims depict little variation, from 0.51178 to 0.51189 (n = 37), corresponding to εNd_{530Ma} between −3.6 and −1.2. We note that the external reproducibility of the εNd values is less than ± 0.7 (2 S.D.; standard deviation), as indicated by measurements of reference materials (ESM Table S5). Initial $^{143}Nd/^{144}Nd$ ratios obtained from the core-rim transition zone are between those from the cores and rims, and likely represent mixed analyzes (Fig. 7m). A profile measured over the rim of grain Mnz28 reveals a systematic increase in the contents of Th (from 7000 to 12300 µg/g) and Y (from 4080 to 6385 µg/g), and in the Th/U ratio (from 850 to 1675) towards the outermost rim (Fig. 7), as well as a decrease in As (from 1990 to 1300 µg/g), and in εHf_{530Ma} (from −1.4 to −2.8). An analogous zoning trend is also obtained for the rim of grain Mnz29 (ESM Table S4). Finally, it is pertinent to note that most rim analyzes show a positive correlation of Th vs. Y (Fig. 7n), and Th vs. ΣHREE (Fig. 7o), whereas the contents of U (approximately 10 µg/g) and Ca (approximately 2000 µg/g) are nearly constant.

Xenotime

Nine measurements for trace elements were carried out on 4 xenotime grains from a heavy-mineral concentrate. The xenotime grains show moderate contents of Th (1247–6412 µg/g) and U (100–817 µg/g), and Th/U ratios that vary from 5.6 to 13. Furthermore, they reveal positive REE fractionation patterns [$(La/Gd)_N$ = 0.00043–0.00063], and relatively low Eu anomalies (Eu^*_N = 0.73–0.80). However, the xenotime grains have higher contents in As (2470–11366 µg/g) and Zr (180–1116 µg/g), in comparison to monazite. For a complete set of major and trace elements see ESM (Tables S3 and S4).

Discussion

Geochronological data

The results of in situ U-Pb dating along with the petrographic observations indicate that the micaschist layer contains detrital grains of zircon, monazite and rutile with a wide range of ages, as well as authigenic grains and overgrowths newly formed and/or recrystallized during a Cambrian event. The detrital grains of zircon and monazite provide evidence for a maximum age of deposition at ca. 1150 Ma, whereas the monazite overgrowths and xenotime point to a metamorphic overprint at ca. 530 Ma. The maximum depositional age is constrained by a concordia age of 1146.9 ± 6.9 Ma (n = 5), resulting from multiple analyzes of the youngest detrital zircon grain (Fig. 4b), and by a $^{206}Pb/^{238}Pb$ age of 1138 ± 14 Ma, obtained from a detrital monazite core (g36c-U26; ESM Table S2). Both ages are only slightly younger than a $^{207}Pb/^{206}Pb$ age of 1176 ± 22 Ma (SHRIMP), previously determined by Chemale et al. (2012) from the youngest zircon grain that was recovered from the phyllitic matrix of the Sopa-Brumadinho metaconglomerate, about 30 m away from the schist layer. All data together confirm that the diamond-bearing Sopa-Brumadinho gravels in the Diamantina region were deposited during the Stenian or later, and form part of the Upper Espinhaço Supergroup, as already proposed by Chemale et al. (2012).

The age spectrum of detrital zircon indicates that the Sopa-Brumadinho metaconglomerate was supplied from a hinterland mainly affected by magmatic events during the Paleoproterozoic, as indicated by prominent age peaks at 1820, 1900, 2000 and 2160 Ma, and minor peaks at 1560, 1740, 2270 and 2390 Ma (Fig. 4c). In addition, the age spectrum provides evidence for magmatic events during the Archean at 3030, 2920 and 2630–2710 Ma, and during the Mesoproterozoic at 1240 and 1150 Ma. A similar zircon age spectrum, although much less diverse, was also reported

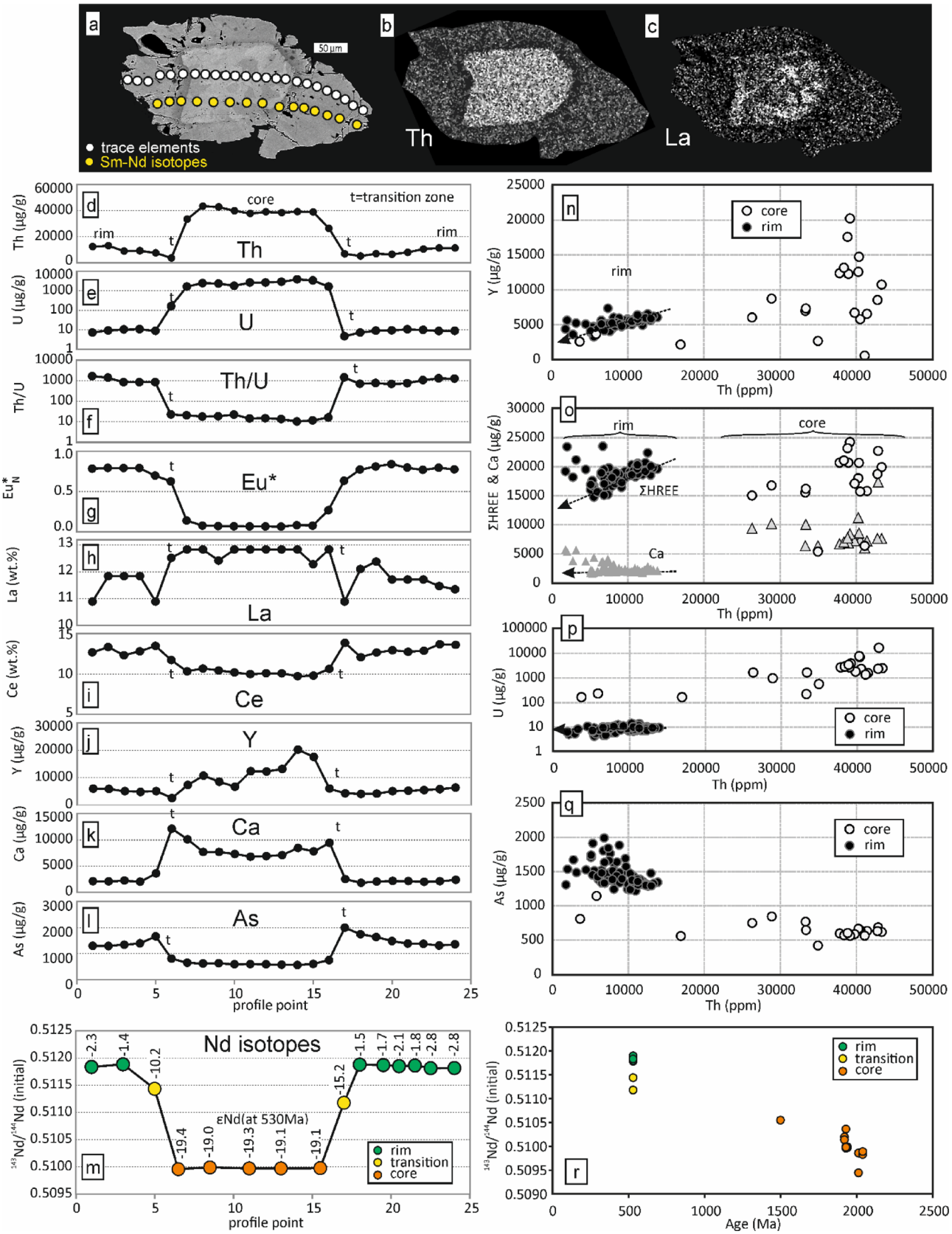
a
50 µm
trace elements
Sm-Nd isotopes
b
Th
c
La
d
Th (µg/g)
core
t=transition zone
rim
t
Th
e
U (µg/g)
U
f
Th/U
Th/U
g
Eu*N
Eu*
h
La (wt.%)
La
i
Ce (wt.%)
Ce
j
Y (µg/g)
Y
k
Ca (µg/g)
Ca
l
As (µg/g)
As
profile point
m
Nd isotopes
εNd(at 530Ma)
-2.3
-1.4
-10.2
-19.4
-19.0
-19.3
-19.1
-19.1
-15.2
-1.5
-1.7
-2.1
-1.8
-2.8
-2.8
143Nd/144Nd (initial)
rim
transition
core
profile point
n
Y (µg/g)
core
rim
rim
Th (ppm)
o
ΣHREE & Ca (µg/g)
rim
core
ΣHREE
Ca
Th (ppm)
p
U (µg/g)
core
rim
Th (ppm)
q
As (µg/g)
core
rim
Th (ppm)
r
143Nd/144Nd (initial)
rim
transition
core
Age (Ma)

Fig. 7 Composition and zoning of monazite. **a** BSE image and **b**, **c** element distribution maps for Th and La of monazite grain Mnz28, as well as laser spot positions for trace element and Sm-Nd isotope analyzes presented in the profiles (**d**–**m**). **n**–**r** Composition of monazite cores and rims of all investigated grains presented in the diagrams: **n** Th vs. Y, **o** Th vs. ΣHREE, and Ca, **p** Th vs. U, **q** Th vs. As, and **r** initial $^{143}Nd/^{144}Nd$ vs. age. The arrows in **n**–**p** highlight correlations mentioned in text. All εNd values [numbers with negative sign in (**m**)] are calculated for an age of 530 Ma

by Chemale et al. (2012). The 12 U-Pb analyzes of detrital monazite cores yield ages between 2270 and 1140 Ma. Most monazite cores formed during Paleoproterozoic magmatic-metamorphic events between 2030 and 1900 Ma, and two grains during Mesoproterozoic events at 1560 and 1140 Ma (Fig. 4c). A Paleoproterozoic event at 1964 ± 17 Ma is also recorded by a grain of detrital rutile.

The age of metamorphic overprint is reflected by a weighted mean $^{206}Pb/^{238}U$ of 531.0 ± 3.4 Ma, obtained from 15 measurements of xenotime (Fig. 5e). This age is within uncertainty identical to a lower-intercept U-Pb age of 531 ± 27 Ma, derived from monazite rims, which compared to xenotime contain much higher contents of common Pb [median value for xenotime: ^{206}Pbc = 3.8% (1.9 to 23%), n = 17; median monazite: ^{206}Pbc = 50% (3.5 to 86%), n = 68)]. Together, the monazite and xenotime analyzes define a regression line with a lower intercept at 530.1 ± 6.0 (MSWD = 2.2; n = 78/86; Fig. 5b). We note that the monazite and xenotime ages are significantly younger than a lower-intercept age of 634 ± 19 Ma, previously obtained from altered grains of detrital zircon from the Paramirim Corridor of the northern Serra do Espinhaço (Franz et al. 2014). However, our monazite and xenotime ages overlap with a $^{207}Pb/^{206}Pb$ age of 524 ± 16 Ma for rutile from an auriferous kaolinite-quartz lode near the town of Diamantina (Cabral et al. 2013). This age is only slightly older than U-Pb ages of metamorphic zircon and rutile, and hydrothermal xenotime and monazite from different amphibolite-facies rocks and hydrothermal veins, respectively, of the Quadrilátero Ferrífero– e.g., the Sitio Lago amphibolite (zircon: 500.6 ± 4.3 Ma; rutile: 499.2 ± 2.9 Ma; Cabral and Zeh 2015a), auriferous tourmaline-rich lode at Passagem de Mariana (xenotime: 496.3 ± 2.0 Ma; Cabral and Zeh 2015b), auriferous quartz-hematite (jacutinga) lode from the Itabira district (monazite: 495.6 ± 2.2 Ma; Cabral et al. 2015a), and different locations of the southern portion of the Quadrilátero Ferrífero (detrital and hydrothermal grains of rutile: 489.4–531.3 Ma; TIMS ages; Santos et al. 2020). Our new ages indicate that the metamorphic overprint of the Diamantina region occurred rather at the end than at the beginning of the Brasiliano orogeny, ca. 600 Ma after the deposition of the Sopa-Brumadinho gravels.

Fluid-rock interaction

The combined results not only demonstrate that detrital grains of zircon, monazite and rutile survived the tectonic-metamorphic overprint during the Brasiliano orogeny, but also that all three minerals in addition to xenotime were newly formed by aqueous fluid-rock interaction. The abundance of detrital grains and the core-rim relationships reported here show that detrital zircon has been best preserved during alteration, followed by monazite and rutile, whereas all xenotime grains are of authigenic origin.

All **zircon** grains analyzed show large detrital cores, commonly surrounded by very thin rims of authigenic origin (< 10 µm in thickness). Only a few cores are strongly altered, displaying porous domains filled with secondary minerals– e.g., xenotime and muscovite (Fig. 3f). The degree of zircon surface dissolution during the metamorphic overprint is hard to assess, as the original shape of most grains is unknown. Nevertheless, fluid-rock interaction must have been pervasive on hand-specimen scale, as nearly all of the approximately 200 grains that were randomly selected for this study show dissolution pits in contact with phengitic muscovite (ESM Figs. S3 and S4). Detrital zircon dissolution is obviously related to the formation of (1) porous zircon domains, which occur behind sharp reaction fronts separating altered from unaltered zircon domains (Fig. 3h), but also to (2) irregular outgrowths limited by phengitic muscovite (Fig. 3a, e). The sharp reaction fronts suggest that detrital zircon is replaced by a CDR process (Putnis 2002; Putnis and Putnis 2007; Geisler et al. 2007), whereas the outgrowths represent either relics of incompletely dissolved zircon, or newly precipitated zircon in the interstices of muscovite crystals. The zircon-muscovite intergrowths suggest that zircon dissolution-reprecipitation was controlled by Zr-Si-K complexes, which likely behave similar to Zr-Si-Na complexes that were experimentally studied by Wilke et al. (2012). These authors demonstrated that aqueous fluids with $NaSi_3$ contents of 10 wt% (formed by incongruent dissolution of albitic feldspar) can dissolve and transport more than 100 µg/g Zr at 600 °C and 0.3 GPa, and even higher contents at lower P-T conditions, but also that Zr-Si-Na complexes are stable at high Na^+/Al^{3+} ratio, and become unstable when the Na^+/Al^{3+} ratio decreases. In the investigated sample, Na-rich fluids obviously played no role because plagioclase is absent, and phengitic muscovite only contains very low Na contents (< 0.025 a.p.f.u.). However, assuming that Zr-Si-K complexes behave similarly to Zr-Si-Na complexes, the zircon outgrowths can be explained by a competitive interplay between fluid transport and muscovite growth in contact with detrital zircon grains. As muscovite is the only sink for Al and K in our sample, progress in phengitic muscovite growth [composition: $KAl_{1.5}(Fe, Mg)_{0.}$

$_5Si_{3.5}Al_{0.5}O_{10}(OH)_2$] would increase the K^+/Al^{3+} ratio of the fluid along the zircon-muscovite interface, as muscovite fixes the double amount of Al^{3+} compared to K^+. Thus, if fluid recharge is hindered or slow compared to muscovite growth, the formation of Zr-Si-K complexes, and, consequently, zircon dissolution is enhanced. On the other hand, if muscovite growth stops, or fluid recharging is fast, Zr-Si-K complexes become unstable, causing the precipitation of the zircon outgrowths recorded in the sample (Fig. 3). We note that some of the Zr-bearing complexes were precipitated away from the dissolved detrital zircon, as indicated by sprays of nanocrystals of authigenic zircon in the muscovite matrix (Fig. 3g). Such zircon nanocrystals point to a DTR process.

Xenotime spatially associated with zircon outgrowths, but also in pores and fractures of altered detrital zircon grains most likely result from the release of HREE, including Y, from zircon during fluid-zircon interaction. This effect has already been described in detail by Franz et al. (2015), although no tetrad effect (Peppard et al. 1969) was observed in our sample. Our observations require that the fluid phase was not only enriched in P, but also in Ti, needed to form xenotime together with rutile within the zircon outgrowths (Fig. 3c, h), and in K, Al, Mg and Fe as well. The latter elements are demanded for the coprecipitation of phengitic muscovite. The source of P might have been detrital apatite, monazite and/or zircon. While detrital apatite was mostly dissolved during fluid rock-interaction, only a few grains of apatite are preserved as inclusions in detrital zircon grains, detrital monazite survived. Higher Th/U ratios of xenotime (Th/U = 5.6–13; median = 7.0), compared to detrital zircon (Th/U = 0.13–1.8; median = 0.56), additionally indicate that U was fractionated from Th during authigenic xenotime growth at the expense of zircon (Fig. 3b, c). This fractionation might be explained either by the involvement of an oxidizing fluid (preferentially removing U^{4+}), or alternatively by the coprecipitation of abundant authigenic rutile (Fig. 3c, h). It is well known that rutile incorporates U, but expels Th during crystallization (Zack et al., 2002, 2011; Luvizotto et al. 2009), causing an increase in the Th/U ratio of the coexisting fluid or melt (Gudelius et al. 2020). Nevertheless, U fractionation by rutile seems to be less likely in our sample, particularly if we consider that the authigenic rutile grains are not perfect crystals, but highly nanoporous aggregates (Fig. 2d, e), with Th/U ratios up to 5.1 (ESM Table S3). Similar features were already discussed in Zeh et al. (2018) and Cabral and Zeh (2023). Finally, we note that no evidence has been found for the preservation of detrital, diagenetic or prograde xenotime in our sample, although such grains were observed widespread in other siliciclastic (meta)sediments (e.g., Lan 2022, and referenced therein), and are predicted to be stable during the prograde metamorphic evolution in typical metapelitic rocks (Spear and Pyle, 2010). Either such grains did never exist or, alternatively, were completely reworked by a DTR process during zircon dissolution accompanied by xenotime precipitation in contact with phengite muscovite.

Detrital monazite cores of round shape, demarcated by a narrow transition zone with numerous muscovite inclusions (Figs. 2g, h and 7a) followed by a monazite rim, hint that monazite was partly dissolved in contact with phengitic muscovite, like detrital zircon, prior to new monazite overgrowth. New growth is constrained by two lines of evidence: (1) the enormous differences in initial $^{143}Nd/^{144}Nd$ between monazite cores and rims; and (2) the nearly identical εNd_{530Ma} values (from −1.4 to −2.8) for all analyzed rims ($n = 21$) that were randomly selected (Fig. 7m, r). The second point indicates that the rims result from a DTR process, comprising: (i) dissolution of detrital monazite (± apatite) grains, (ii) distant fluid transport and homogenization of HFSE and Nd isotopes (at least on hand-specimen scale); and (iii) precipitation of new monazite rims around corroded cores. The same process was already proposed for the homogenization of the Hf isotopic system during metamorphic zircon growth from aqueous fluids under amphibolite-facies conditions (Zeh et al. 2010a; Zeh and Gerdes, 2014), and recently for the Nd isotopic system at metamorphic temperatures between 500 and 700 °C by Biget et al. (2024). We note that a DTR process is quite different to a CDR process, the latter causing an in situ, pseudomorphic alteration of minerals along sharp reaction fronts (see zircon; Fig. 3h), but being unable to homogenize Hf or Nd isotope systems on hand-specimen scale (Zeh et al. 2010a). A CDR process was previously suggested by Rasmussen and Muhling (2007) to explain the core-rim relationships of monazite grains in low-grade metasedimentary rocks of the Stirling Range Formation in Western Australia. In contrast to our sample, those monazite grains are euhedral crystals, which show highly irregular reaction fronts, and similar Th/U ratios for detrital cores and altered rims (Fig. 8b). In agreement, they also reveal a significant decrease in U, Th and Y contents from core to rim, trends already noted in other studies (e.g., Poitrasson et al. 2000; Zi et al. 2024).

Very low contents of U (4–14 µg/g) and extremely high Th/U ratios (400–1675) of the monazite rims in our sample indicate that U was highly fractionated from Th, and removed from the system either before or during the authigenic growth of monazite. The data suggest that the rims precipitated from a highly oxidizing fluid, which causes the removal of hexavalent U while quadrivalent Th remained, an interpretation already applied to explain high Th/U ratios of monazite in Alpine hydrothermal clefts (Janots et al. 2012; Gnos et al. 2015; Grand'Homme et al. 2016), although the interpretation may not be as simple. We note that monazite

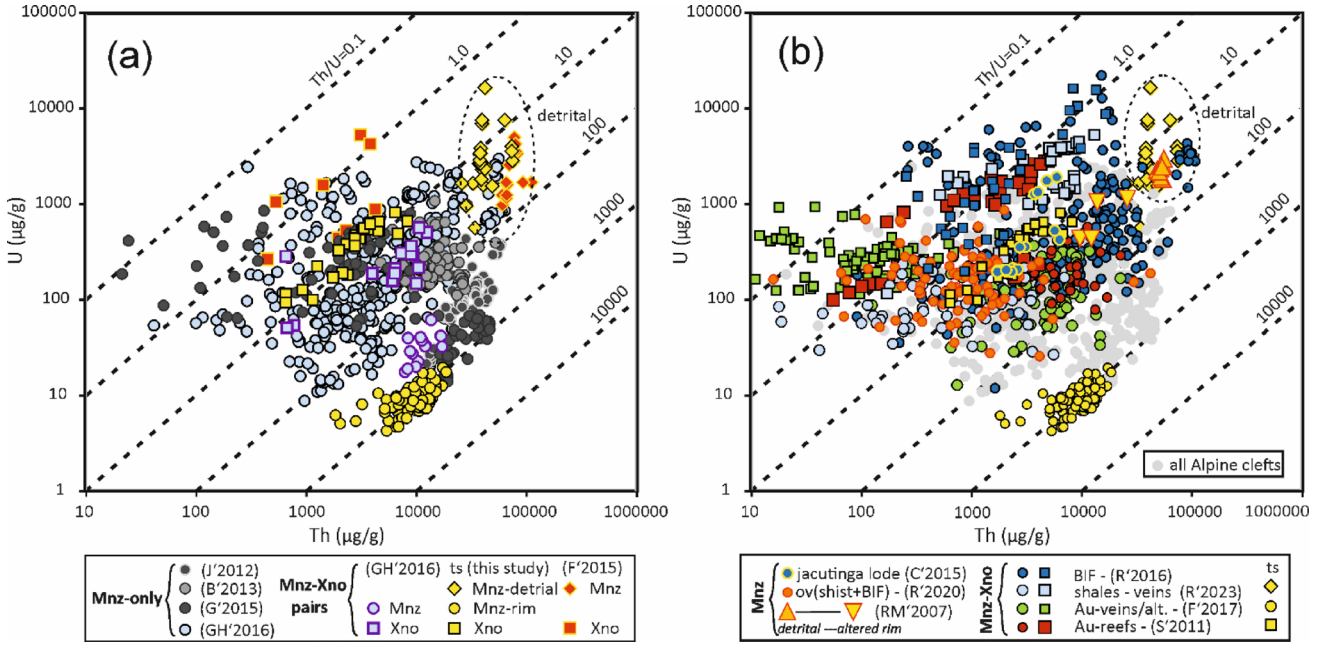

Fig. 8 Comparison of Th-U contents of monazite and xenotime from the southern Serro do Espinhaço (F'2015 - Franz et al. 2015; ts - this study) with such from **a** hydrothermal Alpine clefts (J'2012 - Janots et al. 2012; B'2013– Berger et al. 2013; G'2015– Gnos et al. 2015; GH'2016– Grand'Homme et al. 2016), as well as from a wide range of **b** hydrothermal veins and low-grade rocks, comprising oxidized veins in itabirite (jacutinga lode, Brazil: C'2015– Cabral et al. 2015a), overpressured (ov) schists, hematite-bearing banded-iron formations (BIF), and orogenic Au veins + altered (alt.) country rocks in western Australia (F'2027– Fielding et al. 2017; R'2020 - Rasmussen et al. 2020; R'2023 - Rasmussen et al. 2023), Michigan, USA (R'2016 - Rasmussen et al. 2016), and India (S'2011-Sarma et al. 2011). Furthermore, core-rim relationships of detrital monazite grains hydrothermally altered by a coupled dissolution-reprecipitation process are shown (RM'2007– Rasmussen and Muhling 2007)

with Th/U > 200 is very rare, reported so far only from a small number of Alpine clefts (Janots et al. 2012; Gnos et al. 2015; Grand'Homme et al. 2016; Fig. 9a), but barely from hydrothermal Au-vein systems and low-grade metasedimentary rocks (T < 400°), such as banded iron formations, shales, siltstones and calcareous schists (Fig. 8b). Monazite in all these rocks commonly has U contents of < 1000 µg/g, much lower than monazite in most greenschist- to amphibolite-facies metamorphic rocks (see compilation in Zi et al. 2024). Cleft monazite grains with the highest Th/U ratios (400–1360) typically occur in assemblage with quartz, adularia and chlorite, in addition to minor hematite and rutile/anatase (Janots et al. 2012; Gnos et al. 2015), seldomly with goethite + xenotime (Gnos et al. 2015), or xenotime + allanite + apatite + zircon (Grand'Homme et al. 2016). These mineral assemblages suggest that monazite precipitated from K-Fe-Mg-Al-Ti-REE-P-bearing aqueous fluids, as is also suggested for our monazite. The literature data further indicate that monazite that is spatially associated with hematite and/or goethite does not necessarily show abnormally high Th/U ratios. This, for example, is well reflected by the cleft monazite with Th/U < 10 in the goethite-xenotime-bearing sample Tauern 2 of Gnos et al. (2015), and by monazite in quartz veins rich in specular hematite, i.e., jacutinga lodes, and/or in low-grade metasedimentary rocks, which commonly have Th/U < 100 (see compilation, and references in Fig. 8). This suggests that the Th/U ratio in monazite is not simply controlled by the oxidation state, as reflected by coexisting iron oxides/hydroxides, but also by the availability of U and Th in the fluid at the time of monazite precipitation. In this context, we note that in our sample three mineral phases with high U contents and low Th/U ratios existed at the time of monazite rim growth: (1) detrital zircon (median U = 149 µg/g, Th/U = 0.57, n = 154), (2) detrital monazite (median U = 2274 µg/g, Th/U = 18, n = 24), and (3) authigenic xenotime (median U = 233 µg/g; Th/U = 7.9, n = 9). The detrital zircon and monazite cores were in disequilibrium with the monazite rim, as is reflected by their older ages, whereas the authigenic xenotime and the rim monazite might be cogenetic, an interpretation against which some arguments are presented below.

The enormous differences in U contents and Th/U ratios between authigenic xenotime (median U = 233 µg/g; Th/U = 7.9; n = 9) and the monazite rims (median U = 8.3 µg/g; Th/U = 1057; n = 74; ESM Table S2) hint that both minerals were precipitated from aqueous fluids at different stages of the metamorphic evolution. This interpretation is backed by microfabric relationships indicating that: (1) xenotime was formed during zircon dissolution in contact with phengitic muscovite, the latter representing part of

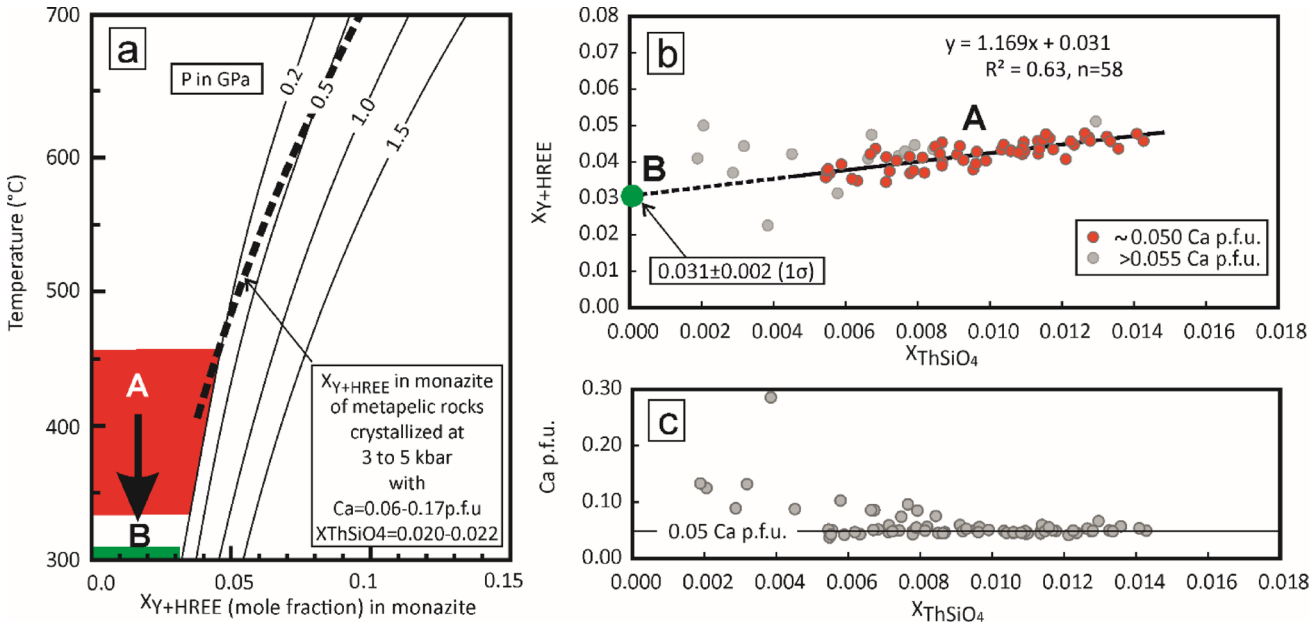

Fig. 9 Results of monazite-xenotime solvus geothermobarometry. **a** X_{Y+HREE} vs. temperature diagram showing the position of the monazite solvus at variable pressures (0.2, 0.5, 1.0, 1.5 GPa; Gratz and Heinrich, 1997), and the solvus (dashed line) presented in Heinrich et al. (1997) for metapelitic rocks at pressures of 0.3–0.5 GPa, and compositions shown in the box. The red field (marked with A) shows the temperature range (at 0.2 GPa) calculated for monazite rims without considering the effect of Th, and the green field (marked with B) by eliminating the effect of Th, using the regression line shown in (**b**). **b**, **c** Composition of monazite rims in the diagrams **b** X_{ThSiO4} vs. X_{Y+HREE} (in mole fraction), and **c** X_{ThSiO4} vs. Ca. The data reveal a positive correlation between Th and Y + HREE at constant Ca content

the peak metamorphic assemblage at T = 510 ± 40 °C, and (2) monazite grew during the retrograde evolution related to the formation of kaolinite at T = 280 ± 30 °C (see section: Temperature-pressure conditions). Nevertheless, crystal-chemical constraints cannot completely be ruled out to account for the observed differences. Literature data show that xenotime in Alpine clefts and low-grade metamorphic rocks mostly have much lower Th/U ratios (factor 10–100) and higher U contents (factor 10) compared to monazite (see compilation in Fig. 8), although monazite-xenotime equilibrium in most samples is not unequivocally proven. Disequilibrium, for example, is well-reflected by significantly different U-Pb ages of monazite (2.30 Ga) and xenotime (2.10–2.05 Ga) occurring side by side within the shale sample investigated by Rasmussen et al. (2023; their Fig. 9), or by xenotime (34.9 ± 0.5 Ma) and monazite (32.3 ± 0.3 Ma) found in a relatively oxidized Alpine cleft (sample MTC of Grand'Homme et al., 2016). Literature data for xenotime-monazite pairs in relatively oxidized Alpine clefts provide a maximum fractionation factor of 13 for Th/U in both minerals [xenotime: median Th/U = 23 (n = 6); monazite: median Th/U = 300 (n = 7); data of Grand'Homme et al. (2016)]. This factor is about 10 times lower than that recorded by the xenotime-monazite pairs of our sample, showing a fractionation factor of 139 (median).

Finally, we note that monazite in our sample shows a systematic increase of the Th/U ratio from the innermost towards the outermost rim, from 700 to 1260 (Fig. 7f), but also in Th and Y contents, indicating a gradual change in the fluid composition during monazite rim growth. This change is also reflected by a systematic decrease in εNd_{530Ma} from −1.3 to −2.8 (Fig. 7m), pointing to a successive dissolution of LREE-rich minerals with low εNd_{530Ma}, perhaps detrital monazite or apatite grains, prior to or during the precipitation of new monazite.

Temperature-pressure conditions

The peak metamorphic temperatures of our sample can be narrowed down on the basis of two important observations. First, quartz-rich domains show microstructures with 120° triple point junctions (Fig. 1a), providing evidence for static recrystallization at temperatures > 400 °C (e.g., Stipp et al., 2002). Second, the age of 1964 ± 17 Ma for the detrital rutile grain indicates that the U-Pb system was not reset by diffusion. This limits the peak temperature to circa 600 °C, in agreement with experimental results for Pb diffusion in rutile (Cherniak, 2000), although Kooijman et al. (2010) suggested a somewhat higher closure temperature of about 650 °C.

Results of the Ti-in-quartz geothermometry of Wark and Watson (2006) yielded temperatures between 463 and 551 °C (mean: 509 ± 40 °C, 1.S.D.; n = 9) for group-1 quartz (Al < 75 µg/g; Ti = 3.2–13 µg/g), whereas for group-2

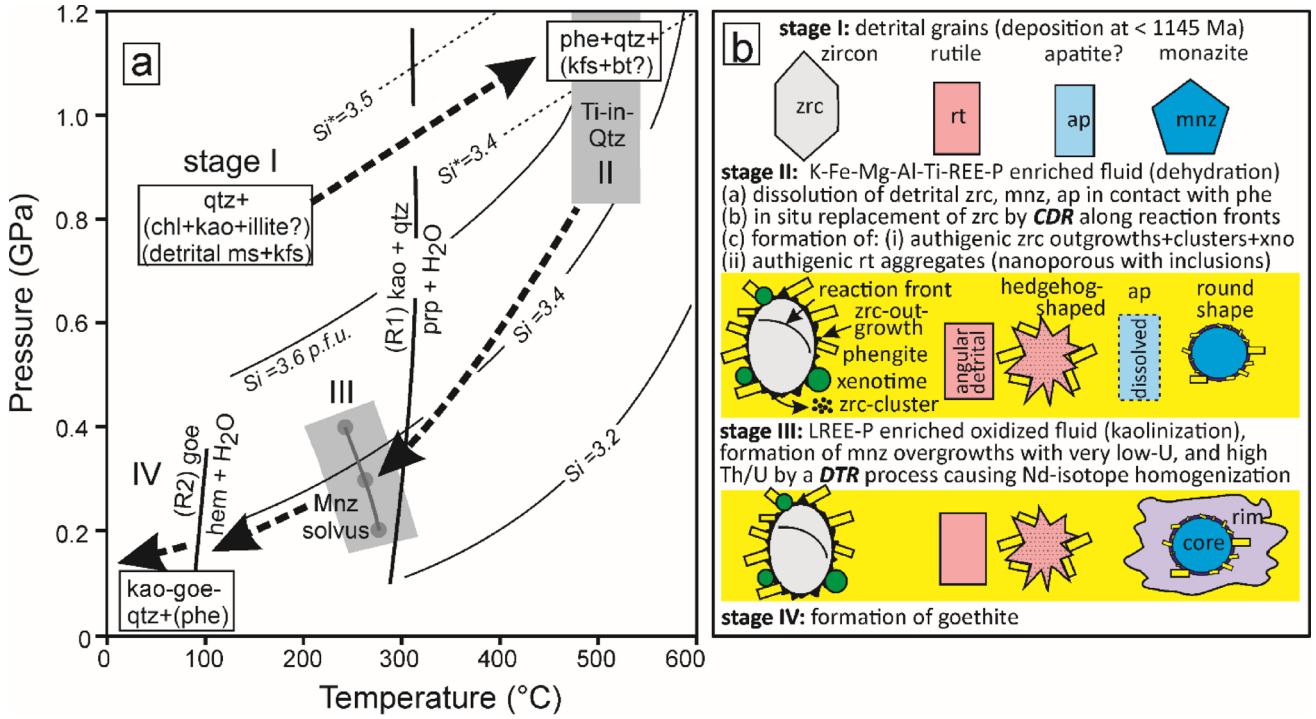

Fig. 10 Synopsis of pressure-temperature-fluid evolution. **a** P-T path (dashed arrows), **b** evolution of the HFSE minerals zircon (zrc), rutile (rt), xenotime (xno), monazite (mnz) and apatite (ap) during different stages of the P-T evolution. The reactions (R1) and (R2) in (**a**) were calculated with the freeware THERMOCALC, using the internally consistent thermodynamic dataset of Holland and Powell (1998). Solid lines marked with Si define the stability limit of phengitic muscovite with Si = 3.2, 3.4, 3.6 a.p.f.u. (atoms per formula unit) in assemblage with K-feldspar-biotite-(chlorite)-quartz, according to Velde (1969). Dotted lines with Si* define the stability limit of phengitic muscovite in the model system KMASH after Massonne and Schreyer (1987). Grey fields - results of Ti-in-Qtz geothermometry and Mnz-Xno solvus geothermobarometry (the points mark variations with pressure increase). Mineral abbreviations: *bt* biotite, *chl* chlorite, *goe* goethite, *hem* hematite, *kao* kaolinite, *kfs* K-feldspar, *ms* muscovite, *phe* phengitic muscovite, *prp* pyrophyllite, *qtz* quartz. *CDR* Coupled Dissolution Reprecipitation, *DTR* Dissolution followed by distant Transport and Reprecipitation of the same mineral species

quartz (Al > 179 µg/g; Ti = 30–88 µg/g) the temperatures are between 630 and 733 °C. These higher temperatures likely result from quartz-hosted TiO_2 (nano)inclusions which were suspected on the basis of microscopic observations (Fig. 1c), but could not be detected by Raman spectrometry and time-resolved signals during LA-ICP-MS analyzes. A wide range of temperatures was also obtained for authigenic rutile by applying the Zr-in-rutile geothermometer of Ferry and Watson (2007), although with significant differences among the rutile types. Rutile grains of type 1 and 2 (both with negative REE fractionation patterns; Fig. 6c) contain the lowest Zr contents (Zr = 30–69 µg/g), which correspond to temperatures between 577 and 640 °C (mean = 608 ± 16, 1.S.D.; $n = 11$). In contrast, rutile grains of type 3 (with positive REE fractionation) show wide variations in Zr, from 84 to 1340 µg/g, corresponding to temperatures between 656 and 1207 °C. It is likely that all Zr-in-rutile temperatures are too high, for the following three reasons: (1) all rutile analyzes, except of the detrital grain, have high contents of rutile-incompatible elements such as Th and REE (ESM Table S3); (2) show nanopores (Fig. 2e); (3) contain nanoinclusions of secondary phases (Fig. 2e). The nanoinclusions are obviously well disseminated within the grains and cannot be detected by LA-ICP-MS analyzes with a spot diameter of 20 µm. During LA-ICP-MS measurements time-resolved signals of rutile-incompatible elements like Th, and REE are always parallel to signals of rutile-compatible elements like Nb (see Fig. 6d). Similar features have already been reported by Zeh et al. (2018). Taken this into account, all Zr-in-rutile temperatures for the authigenic rutile grains are deemed too high, due to excess of Zr, which is not located in the rutile lattice, but rather in interstitial nanopores and/or nanoinclusions.

While the peak temperature is best constrained by the results of Ti-in-Qtz geothermometry (509 ± 40 °C), the pressure is limited by the Si component in phengitic muscovite (3.3–3.6 Si a.p.f.u.). Application of the phengite geothermobarometers of Velde (1967) and Massone and Schreyer (1987) yield pressures between 0.8 and 1.3 GPa at 510 °C (Fig. 10a). However, it is pertinent to note that the application of both geobarometers require that phengitic muscovite occurs in assemblage with K-feldspar and biotite/chlorite, a prerequisite not confirmed by our petrographic observations, as neither K-feldspar nor biotite nor chlorite were

found. Thus, the pressure derived from the Si-in-phengite geobarometer must be considered as a maximum pressure. We further note that the peak P-T conditions derived from this study are similar to those previously obtained by Franz et al. (2015) for rocks of the Diamantina region (T = 550 ± 37° at > 0.6 GPa).

To place additional constraints on the formation of monazite rims, a modified version of the monazite-xenotime solvus geothermobarometer of Gratz and Heinrich (1997) was applied, assuming that the Y + HREE content of monazite is buffered by xenotime (Heinrich et al. 1997). This geothermobarometer, experimentally calibrated for the model system YPO_4-$CePO_4$ at pressures between 0.2 and 1.5 GPa, has the expression:

$$T\,(^\circ C) = 439.75 * \ln\left(\frac{X^{mnz}_{YPO4}}{0.01459 + 0.000852 * P\,(kbar)}\right)$$

Modification was done by exchanging the expression X^{mnz}_{YPO4} for $X^{mnz}_{[Y+HREE(PO4)]}$, which accounts for the substitution of Y by HREE (Gd to Lu) in natural monazite. By assuming a pressure of 2 kbar (≈ 0.2 GPa), temperatures between 330 and 503 °C (mean = 419 ± 39 °C, 1 S.D.; $n = 70$) were obtained. At higher pressure, the calculated temperatures would be lower (Fig. 9a), and if the effect of Th is taken into account. Experiments carried out by Seydoux-Guillaume et al. (2002) showed that the incorporation of Th into monazite lowers the solvus temperature significantly, compared to the pure YPO_4-$CePO_4$ system, due to the incorporation of additional Y via the coupled substitution $Th^{4+} + Si^{4+} = Y^{3+} + P^{5+}$. For the investigated monazites, this substitution is reflected by the positive correlation between X_{ThSiO4} and $X_{(Y+HREE)}$ (Fig. 9b), suggesting that the enormous temperature variations (330–503 °C) are very likely an artefact of Th zoning (Fig. 7n-o). Assuming that all monazite rims are cogenetic, the effect of Th incorporation can be eliminated by applying $X_{ThSiO4} = 0$ to the regression line shown in Fig. 9b. This results in $X_{Y+HREE} = 0.031 \pm 0.002$ (1 S.E., $n = 58$), corresponding to a temperature of 283 ± 28 °C (at 0.2 GPa) or 260 ± 28 °C (at 0.3 GPa) by applying the geothermobarometer of Gratz and Heinrich (1997). The effect of Ca on the solvus geothermometer is negligible, and perhaps minor, as the Ca content of all monazite rims is low and nearly constant (Ca = 0.05 a.p.f.u.; Fig. 9c), except for a few analyzes from the core-rim transition zone.

We note that the temperature calculated for the rim monazite is in good agreement with the observed assemblage kaolinite + quartz, which has an uppermost stability limit of T = 295 ± 7 °C (0.2 GPa) defined by the reaction kaolinite + 2 quartz = pyrophyllite + H_2O (Fig. 10a). Similar P-T conditions of approximately 300 °C at 0.2 GPa were also obtained by a fluid-inclusion study, carried out on rutile grains from an auriferous quartz–kaolinite–hematite vein near the town of Diamantina by Cabral et al. (2015b). We note that kaolinization is a regional phenomenon in the southern Serra do Espinhaço, already mentioned by Correns (1932). In summary, our combined results suggest that the monazite rims in the micaschist were formed by intense fluid-rock interaction during the retrograde P-T evolution. The observed assemblage goethite–kaolinite–quartz further indicates that the fluid overprint continued down to temperatures < 100 °C at < 0.2 GPa (see Babcan 1971; Tardy and Nahon 1985), also implied by the reaction hematite + H_2O = goethite (Fig. 10a).

Conclusions

1. Results of this study show that the HFSE minerals zircon, monazite, xenotime and rutile in micaschist can provide not only information about the timing of sediment deposition and metamorphic overprint, but also about fluid-rock interaction at different stages of the pressure-temperature evolution (Fig. 10b).
2. Detrital zircon, monazite and rutile indicate deposition of diamond-bearing gravels at < 1150 Ma, and detritus supply from a hinterland affected by magmatic and metamorphic overprint mainly between 2160 and 1820 Ma.
3. Authigenic monazite, xenotime, zircon and rutile were formed during the metamorphic-hydrothermal overprint related to the Brasiliano orogeny at ca. 530 Ma.
4. Formation of zircon outgrowths, together with authigenic xenotime and rutile, result from intense leaching of detrital zircon grains in contact to phengitic muscovite close to the metamorphic peak at T = 510 ± 40 °C and $P > 0.8$ GPa.
5. Authigenic rims of monazite were formed during the retrograde evolution at T = 280 ± 30 °C and $P < 0.2$ GPa during kaolinization.
6. Fluid-rock interaction at the metamorphic peak was mainly driven by prograde dehydration reactions of K-Fe-Mg-Ti-Al-bearing phyllosilicates, comprising muscovite, chlorite and/or biotite. The released fluids caused zircon dissolution, transport and precipitation in contact with growing phengitic muscovite, dependent on temporal and spatial variations in K^+/Al^{3+} ratios, affecting the stability of K-Si-Zr complexes. Furthermore, zircon was replaced in situ by a CDR process, and precipitated as clusters elsewhere in the sample by a DTR process, which also caused formation of authigenic rutile aggregates. Xenotime formed as a by-product of zircon dissolution.
7. Retrograde fluid-rock interaction was controlled by the infiltration of oxidized aqueous fluids enriched in

P and LREE, causing partial kaolinization of phengite and new formation of monazite rims with extremely high Th/U ratios (up to 1680) and very low U contents (< 14 µg/g). Neodymium isotope data provide unambiguous evidence for a DTR process, which occurred prior to goethite formation at T < 100 °C.

Supplementary Information The online version contains supplementary material available at https://doi.org/10.1007/s00410-025-02244-2.

Acknowledgements AZ, KD and AG thanks Linda Markow and Aratz Berranoaguirre (both FIERCE Frankfurt am Main) for help with U-Pb dating and Nd-isotope analyzes, and Martin van Dollen (KIT) for thin section and epoxy mount preparation. SL thanks Ulf Hemmerling (TUC) for sample preparation and Dietlind Nordhausen for assistance with EMPA analyzes. Pedro Angelo Almeida Abreu and José Maria Leal (UFVJM) kindly took ARC, AZ and SL to the historical Extração diamond mine. We are further in debt of Daniela Rubatto for editorial handling, and Zhongwu Lan and an anonymous reviewer for constructive reviews.

Author contributions Armin Zeh — Conceptualization, Methodology, Validation, Formal Analysis (sample preparation, heavy mineral separation, petrography, U-Pb-dating, trace element analyzes by LA-SF-ICP-MS), Investigation, Writing, Editing — Original Draft, Visualization, Supervision, Project Administration. Stephanie Lohmeier — Methodology, Validation, Formal Analysis (EPMA analyzes), Investigation, Writing. Alexandre Raphael Cabral — Methodology (sampling and field observation), Validation, Investigation, Writing—Original Draft. Kirsten Drüppel—Investigation, Formal Analyzes (XRD, Raman spectroscopy), Writing— Original Draft. Axel Gerdes Conceptualization, Methodology, Validation, Formal Analysis (in situ Sm-Nd isotope analyzes by LA-MC-ICP-MS), Writing—Original Draft.

Funding Open Access funding enabled and organized by Projekt DEAL.

References

Allaz J, Selleck B, Williams ML, Jercinovic MJ (2013). Microprobe analysis and dating of monazite from the Potsdam Formation, New York: A progressive record of chemical reaction and fluid interaction. Am Min 98: 1106–1119. doi: https://doi.org/10.2138/am.2013.4304

Andò S, Garzanti E, Padoan M, Limonta M (2012) Corrosion of heavy minerals during weathering and diagenesis: A catalog for optical analysis. Sed Geol 280:165–178. https://doi.org/10.1016/j.sedgeo.2012.03.023

Babcan J (1971) Synthesis of Jarosite KFe3(SO4)2(OH)6. Geol. Zb. 22:299–304.

Baldwin JA, Bowring SA, Williams ML, Mahan KH (2006). Geochronological constraints on the evolution of high-pressure felsic granulites from an integrated electron microprobe and ID-TIMS geochemical study. Lithos 88: 173–200. https://doi.org/10.1016/j.lithos.2005.08.009.

Berger A, Gnos E, Janots E, Whitehouse M, Soom M, Frei R, Waight TE (2013) Dating brittle tectonic movements with cleft monazite: fluid-rock interaction and formation of REE minerals. Tectonics 32:1–14. https://doi.org/10.1002/tect.20071

Berry RF, Goemann K, Thompson J, Meffre S, Bottrill R (2018) Geochemistry and provenance of the Turquoise Bluff Slate, northeastern Tasmania: tectonic significance. Australian J Earth Sci 66:227–246. https://doi.org/10.1080/08120099.2019.1541253

Biget T, Bruand E, Pereira I, Boyet M, Gasser D, Stüwe K, Langone A. (2024) The chemical and Sm–Nd isotopic behaviour of accessory minerals in metasediments along the LP-HT Chugach Metamorphic Complex (Alaska). Contrib Mineral Petrol 179, 108. https://doi.org/10.1007/s00410-024-02185-2

Black LP, Williams IS (1986) Four zircon ages from one rock: the history of a 3,930 Ma-old granulite from Mount Sones, Enderby Land, Antarctica. Contrib Mineral Petrol 94:427–437. https://doi.org/10.1007/BF00376336

Bojanowski MJ, Bagiński B, Clarkson E, MacDonald R, Marynowski L (2012) Low-temperature zircon growth related to hydrothermal alteration of siderite concretions in Mississippian shales, Scotland. Contrib Mineral Petrol 164:245–259. https://doi.org/10.1007/s00410-012-0736-6

Cabral AR, Zeh A (2015a) Detrital zircon without detritus: a result of 496-Ma-old fluid–rock interaction during the gold-lode formation of Passagem, Minas Gerais, Brazil. Lithos 212–215:415–427. https://doi.org/10.1016/j.lithos.2014.10.011

Cabral AR, Zeh A (2015b) Celebrating the centenary of "The geology of central Minas Gerais, Brazil": an insight from the Sítio Largo amphibolite. J Geol 123:337–354. https://doi.org/10.1086/682047

Cabral AR, Zeh A (2023) Karst-bauxite formation during the Great Oxidation Event– constraints from dating of authigenic rutile and its thorium content. Scientific Reports 13:8633. https://doi.org/10.1038/s41598-023-35574-x

Cabral AR, Eugster O, Brauns M, Lehmann B, Rösel D, Zack T, de Abreu FR, Pernicka E, Barth M (2013) Direct dating of gold by radiogenic helium: Testing the method on gold from Diamantina, Minas Gerais, Brazil: Geology 41:163–166. https://doi.org/10.1130/G33751.1

Cabral AR, Zeh A, Galbiatti HF, Lehmann B (2015a) Late Cambrian Au–Pd mineralization and Fe enrichment in the Itabira district, Minas Gerais, Brazil, at 496 Ma: constraints from U–Pb monazite dating of a jacutinga lode. Econ Geol 110:263–272. https://doi.org/10.2113/econgeo.110.1.263

Cabral AR, Rios FJ, de Oliveira LAR, de Abreu FR, Lehmann B, Zack T, Laufek F (2015b) Fluid-inclusion microthermometry and the Zr-in-rutile thermometer for hydrothermal rutile. Int J Earth Sci (Geol Rundsch) 104:513–519. https://doi.org/10.1007/s00531-014-1120-8

Chemale FJ, Dussin IA, Alkmim FF, Martins MS, Queiroga G, Armstrong R, Santos MN (2012) Unravelling a Proterozoic basin history through detrital zircon geochronology: The case of the Espinhaço Supergroup, Minas Gerais, Brazil. Gondwana Res 22:200–206. https://doi.org/10.1016/j.gr.2011.08.016

Cherniak DJ, Watson EB (2001) Pb Diffusion in zircon. Chem Geol 172:5–24. https://doi.org/10.1016/S0009-2541(00)00233-3

Cherniak DJ, Watson EB, Grove M, Harrison TM (2004) Pb diffusion in monazite: a combined RBS/SIMS study. Geochim Cosmochim Acta 68:829–840. https://doi.org/10.1016/j.gca.2003.07.012

Cherniak DJ (2000) Pb diffusion in rutile. Contrib Mineral Petrol 139:198–207. https://doi.org/10.1007/PL00007671

Cherniak DJ (2006) Pb and rare earth element diffusion in xenotime. Lithos 88:1–14. https://doi.org/10.1016/j.lithos.2005.08.002

Copeland P, Parrish R, Harrison T (1988) Identification of inherited radiogenic Pb in monazite and its implications for U–Pb systematics. Nature 333:760–763. https://doi.org/10.1038/333760a0

Correns CW (1932) Über die Diamantlagerstätten des Hochlandes von Diamantina, Minas Geraes, Brasilien. Zeitschrift für praktische Geologie 40:161–168, 177–181.

Ferry JM, Watson EB (2007) New thermodynamic models and revised calibrations for the Ti-in-zircon and Zr-in-rutile thermometers. Contrib Mineral Petrol 154:429–437. https://doi.org/10.1007/s00410-007-0201-0

Fielding IOH, Johnson SP, Zi J-W, Rasmussen B, Muhling JR, Dunkley DJ, Sheppard S, Wingate MTD, Rogers JR (2017) Using In Situ SHRIMP U-Pb Monazite and Xenotime Geochronology to Determine the Age of Orogenic Gold Mineralization: An Example from the Paulsens Mine, Southern Pilbara Craton. Econ Geol 112: 1205–1230. https://doi.org/10.5382/econgeo.2017.4507

Franz G, Morteani G, Gerdes A, Rhede D (2014) Ages of protolith and Neoproterozoic metamorphism of Al–P-bearing quartzites of the Veredas formation (Northern Espinhaço, Brazil): LA–ICP–MS age determinations on relict and recrystallized zircon and geodynamic consequences. Precam Res 250:6–26. https://doi.org/10.1016/j.precamres.2014.05.011

Franz G, Morteani G, Rhede D (2015) Xenotime-(Y) formation from zircon dissolution–precipitation and HREE fractionation: an example from a metamorphosed phosphatic sandstone, Espinhaço fold belt (Brazil). Contrib Mineral Petrol 170:37. https://doi.org/10.1007/s00410-015-1191-y

Geisler T, Schaltegger U, Tomaschek F (2007) Re-equilibration of zircon in aqueous fluids and melts. Elements 3:45–51. https://doi.org/10.2113/gselements.3.1.43

Gnos E, Janots E, Berger A, Whitehouse M, Walter F, Pettke T, Bergemann C (2015) Age of cleft monazites in the eastern Tauern Window: constraints on crystallization conditions of hydrothermal monazite. Swiss J Geosci 108:55–74. https://doi.org/10.1007/s00015-015-0178-z

Grand'Homme A, Janots E, Bosse V, Seydoux-Guillaume AM, De Ascenção Guedes R (2016) Interpretation of U-Th-Pb in situ ages of hydrothermal monazite-(Ce) and xenotime-(Y): evidence from a large-scale regional study in clefts from the western alps. Miner Petrol 110:787–807. https://doi.org/10.1007/s00710-016-0451-5

Gratz R, Heinrich W (1997) Monazite-xenotime thermobarometry: experimental calibration of the miscibility gap in the binary system CePO4-YPO4. Am Mineral 82:772–780. https://doi.org/10.2138/am-1997-7-816

Gudelius D, Zeh A, Wilson AH (2020) Zircon formation in mafic and felsic rocks of the Bushveld Complex (South Africa): constraints from composition, zoning, Th/U ratios, morphology, and modelling. Chem Geol 546:119647. https://doi.org/10.1016/j.chemgeo.2020.119647

Harlov D, Wirth R, Hetherington CJ (2011) Fluid-mediated partial alteration in monazite: the role of coupled dissolution-reprecipitation in element redistribution and mass transfer. Contrib Mineral Petrol 162:329–348. https://doi.org/10.1007/s00410-010-0599-7

Hay DC, Dempster TJ (2009) Zircon alteration, formation and preservation in sandstones. Sedimentology 56:2175–2191. https://doi.org/10.1111/j.1365-3091.2009.01075.x

Hay DC, Dempster TJ, Lee MR, Brown DJ (2010) Anatomy of a low temperature zircon outgrowth. Contrib Mineral Petrol 159:81–92. https://doi.org/10.1007/s00410-009-0417-2

Heinrich W, Andrehs G, Franz G (1997) Monazite-xenotime miscibility gap thermometry: I. An empirical calibration. J metamorphic Geol 15:3–17. https://doi.org/10.1111/j.1525-1314.1997.t01-1-00052.x

Holland TJB, Powell R (1998) An internally consistent thermodynamic data set for phases of petrological interest. J metamorph Geol 16: 309–343. https://doi.org/10.1111/j.1525-1314.1998.00140.x

Hubert JF (1962) A zircon-tourmaline-rutile maturity index and the interdependence of the composition of heavy mineral assemblages with the gross composition and texture of sandstones. J Sediment Res 32:440–450. https://doi.org/10.1306/74d70ce5-2b21-11d7-8648000102c1865d

Janots E, Berger A, Gnos E, Whitehouse MJ, Lewin E, Pettke T (2012) Constraints on fluid evolution during metamorphism from U–Th–Pb systematics in Alpine hydrothermal monazite. Chem Geol 326:61–71. https://doi.org/10.1016/j.chemgeo.2012.07.014

Kooijman E, Mezger K, Berndt J (2010) Constraints on the U–Pb systematics of metamorphic rutile from in situ LA-ICP-MS analysis. Earth Planet Sci Lett 293: 321–330. https://doi.org/10.1016/j.epsl.2010.02.047

Krenn E, Finger F (2007) Formation of monazite and rhabdophane at the expense of allanite during Alpine low temperature retrogression of metapelitic basement rocks from Crete, Greece: microprobe data and geochronological implications. Lithos 95: 130–147. https://doi.org/10.1016/j.lithos.2006.07.007

Lan Z (2022) Authigenic monazite and xenotime Pb-Pb/U-Pb dating of siliciclastic sedimentary rocks, Earth-Sci Rev 234: 104217. https://doi.org/10.1016/j.earscirev.2022.104217

Lan Z, Li XH, Chen ZQ, Li QL, Hofmann A, Zhang YB, Zhong Y, Liu Y, Tang GQ, Ling XX, Li J (2014) Diagenetic xenotime age constraints on the Sanjiaotang Formation, Luoyu Group, southern margin of the North China Craton: Implications for regional stratigraphic correlation and early evolution of eukaryotes. Precam Res 251:21–32. https://doi.org/10.1016/j.precamres.2014.06.012

Luvizotto GL, Zack T, Meyer HP, Ludwig T, Triebold S, Kronz A, Münker C, Stockli DF, Prowatke S, Klemme S, Jacob DE, von Eynatten H (2009) Rutile crystals as potential trace element and isotope mineral standards for microanalysis. Chem Geol 261:346–369. https://doi.org/10.1016/j.chemgeo.2008.04.012

Massonne HJ, Schreyer W (1987) Phengite geobarometry based on the limiting assemblage with K-feldspar, phlogopite, and quartz. Contrib Miner Petrol 96:212–224. https://doi.org/10.1007/BF00375235

Meinhold G (2010) Rutile and its applications in earth sciences. Earth-Sci Rev 102:1–28. https://doi.org/10.1016/j.earscirev.2010.06.001

Moraes LJ, Guimarães D (1931) The diamond-bearing region of northern Minas Geraes, Brazil. Econ Geol 26:502–530. https://doi.org/10.2113/gsecongeo.26.5.502

Morton AC, Hallsworth C (1994) Identifying provenance-specific features of detrital heavy mineral assemblages in sandstones. Sedimentary Geol 90:241–256. https://doi.org/10.1016/0037-0738(94)90041-8

Morton AC, Hallsworth C (2007) Chap. 7 stability of detrital heavy minerals during burial diagenesis. In MA Mange and DT Wright (Eds), Developments in Sedimentology 58:215–245. Elsevier. https://doi.org/10.1016/S0070-4571(07)58007-6

Peppard DF, Mason GW, Lewey S (1969) A tetrad effect in the liquid-liquid extraction ordering of the lanthanides(III). J Inorganic Nuclear Chem 31:2271–2272. https://doi.org/10.1016/0022-1902(69)90044-X

Poitrasson F, Chenery S, Shepherd TJ (2000) Electron microprobe and LA-ICP-MS study of monazite hydrothermal alteration: Implications for U-Th-Pb geochronology and nuclear ceramic. Geochim Cosmochim Acta 64:3283–3297. https://doi.org/10.1016/S0016-7037(00)00433-6

Putnis A, Putnis CV (2007) The mechanism of reequilibration of solids in the presence of a fluid phase. J Solid State Chem 180:1783–6. https://doi.org/10.1016/j.jssc.2007.03.023

Putnis A (2002) Mineral replacement reactions: from macroscopic observations to microscopic mechanisms. Min Mag 66:689–708. https://doi.org/10.1180/0026461026650056

Rasmussen B (2005) Zircon growth in very low grade metasedimentary rocks: evidence for zirconium mobility at ~250°C. Contrib Mineral Petrol 150:146–155. https://doi.org/10.1007/s00410-005-0006-y

Rasmussen B, Muhling JR (2007) Monazite begets monazite: evidence for dissolution of detrital monazite and reprecipitation of syntectonic monazite during low-grade regional metamorphism. Contrib Mineral Petrol 154:675–689. https://doi.org/10.1007/s00410-007-0216-6

Rasmussen B, Bengtson S, Fletcher IR, McNaughton NJ (2002). Discoidal impressions and trace-like fossils more than 1200 million years old. Science 296:1112-5. https://doi:10.1126/science.1070166

Rasmussen B, Zi J-W, Sheppard S, Krapež B, Muhling JR (2016) Multiple episodes of hematite mineralization indicated by U-Pb dating of iron-ore deposits, Marquette Range, Michigan, USA. Geology 44:547–550. https://doi.org/10.1130/G37783.1

Rasmussen B, Zi J-W, Muhling JR, Dunkley DJ, Fischer WW (2020) U-Pb dating of overpressure veins in late Archean shales reveals six episodes of Paleoproterozoic deformation and fluid flow in the Pilbara craton. Geology 48:961–965. https://doi.org/10.1130/G47526.1

Rasmussen B, Zi J-W, Muhling JR (2023) Tectonic fluid expulsion: U-Pb evidence for punctuated hydrothermal fluid flow and hydraulic fracturing during orogenesis. Earth Planet Sci Lett 604:117997. https://doi.org/10.1016/j.epsl.2023.117997

Santos MM, Lana C, Scholz R, Buick IS, Kamo SL, Corfu F, Queiroga G (2020) LA-ICP-MS U–Pb dating of rutiles associated with hydrothermal mineralization along the southern Araçuaí Belt, SE Brazil, J South Am Earth Sci 99:102502. https://doi.org/10.1016/j.jsames.2020.102502

Sarma DS, Fletcher IR, Rasmussen B, McNaughton NJ, Mohan MR, Groves DI (2011) Archaean goldmineralization synchronous with late cratonization of the Western Dharwar Craton, India: 2.52 Ga U–Pb ages of hydrothermal monazite and xenotime in gold deposits. Miner Deposita 46:273–288. https://doi.org/10.1007/s00126-010-0326-3

Sengupta, D., Van Gosen BS (2016) Placer-Type Rare Earth Element Deposits (in: Philip L. Verplanck, PL, Hitzman, MW (eds) Rare Earth and Critical Elements in Ore Deposits. Rev. in Econ. Geol. 8: https://doi.org/10.5382/REV.18

Seydoux-Guillaume A-M, Wirth R, Heinrich W, Montel JM (2002) Experimental determination of Thorium partitioning between monazite and xenotime using analytical electron microscopy and X-ray diffraction Rietveld analysis. Eur J Mineral 14:869–878. https://doi.org/10.1127/0935-1221/2002/0014-0869

Spear FS, Pyle JM (2010) Theoretical modeling of monazite growth in a low-Ca metapelite. Chem Geol 273:111–119. https://doi.org/10.1016/j.chemgeo.2010.02.016.

Stipp M, Stünitz H, Heilbronner R, Schmid SM (2002). The eastern Tonale fault zone: a 'natural laboratory' for crystal plastic deformation of quartz over a temperature range from 250 to 700°C, J Structural Geol 24:1861–1884.

Tardy Y, Nahon D (1985) Geochemisty of laterites, stability of Al-Goethite, Al-Hematite and Fe3+-kaolinite in bauxites and Ferricretes; an approach to the mechanism of concretion formation. Am J Sci 285:865–903. https://doi.org/10.2475/ajs.285.10.865 .865

Velde B (1967) Si^{4+} content of natural phengites. Contrib Mineral Petrol 14:250–258. https://doi.org/10.1007/BF00376643

Wark DA, Watson EB (2006) TitaniQ: a titanium-in-quartz geothermometer. Contrib Mineral Petrol 152:743–754. https://doi.org/10.1007/s00410-006-0132-1

Wilke M, Schmidt C, Dubrail J, Appel K, Borchert M, Kvashnina K, Manning CE (2012) Zircon solubility and zirconium complexation in $H_2O+Na_2O+SiO_2\pm Al_2O_3$ fluids at high pressure and temperature. Earth Planet Sci Lett 349–350:15–25. https://doi.org/10.1016/j.epsl.2012.06.054

Zack T, Stockli DF, Luvizotto GL, Barth MG, Belousova E, Wolfe MR, Hinton RW (2011) In situ U–Pb rutile dating by LA–ICP–MS: ^{208}Pb correction and prospects for geological applications: Contrib Mineral Petrol 162:515–530. https://doi.org/10.1007/s00410-011-0609-4

Zack T, Kronz A, Foley SF, Rivers T (2002). Trace element abundances in rutiles from eclogites and associated garnet mica schists. Chem Geol 184:97–122. https://doi.org/10.1016/S0009-2541(01)00357-6

Zeh A, Gerdes A (2014) HFSE-transport and U-Pb-Hf isotope homogenization mediated by Ca-bearing aqueous fluids at 2.04 Ga: constraints from zircon, monazite, and garnet of the Venetia Klippe, Limpopo Belt, South Africa. Geochim Cosmochim Acta 138:81–100. https://doi.org/10.1016/j.gca.2014.04.015

Zeh A, Millar IL, Horstwood MSA (2004) Polymetamorphism in the NE Shackleton Range, Antarctica: constraints from petrology and U-Pb, Sm-Nd, Rb-Sr TIMS and in situU-Pb LA-PIMMS dating. J Petrol 45:949–973. https://doi.org/10.1093/petrology/egg117

Zeh A, Gerdes A, Will TM, Frimmel H (2010a) Hafnium isotope homogenization during metamorphic zircon growth in amphibolite-facies rocks, examples from the Shackleton Range (Antarctica). Geochim Cosmochim Acta 74:4740–4758. https://doi.org/10.1016/j.gca.2010.05.016

Zeh A, Gerdes A, Barton JM Jr, Klemd R (2010b) U-Th-Pb and Lu-Hf systematics of zircon from TTG's, leucosomes, anorthosites and quartzites of the Limpopo Belt (South Africa): constraints for the formation, recycling, and metamorphism of Paleoarchean crust. Precam Res 179:50–68. https://doi.org/10.1016/j.precamres.2010.02.012

Zeh A, Cabral A, Koglin N, Decker M (2018) Rutile alteration and authigenic growth in metasandstones of the Moeda Formation, Minas Gerais, Brazil - a result of Transamazonian fluid-rock interaction. Chem Geol 483:397–409. https://doi.org/10.1016/j.chemgeo.2018.03.007

Zhang YB, Li QL, Lan ZW, Wu FY, Li XH, Yang JH, Zhai MG (2015) Diagenetic xenotime dating to constrain the initial depositional time of the Yan-Liao Rift. Precam Res 271:20–32. https://doi.org/10.1016/j.precamres.2015.09.024

Zhang SJ, Cao R, Lan ZW, Li ZS, Zhao ZY, Wan B, Guan CG, Yuan XL (2022) SIMS Pb-Pb dating of phosphates in the Proterozoic strata of SE North China Craton: Constraints on eukaryote evolution. Precam Res 371:106562. https://doi.org/10.1016/j.precamres.2022.106562

Zi J-W, Muhling JR, Rasmussen R (2024). Geochemistry of low-temperature (<350°C) metamorphic and hydrothermal monazite. Earth-Science Reviews 249:104668.